TRAVEL-TIME SEISMIC INVERSION FOR A NUMERICALLY-DEFINED SHAPE

JOEL P. KOOPS

Travel-time seismic inversion for a numerically-defined shape

by

Joel P. Koops

A thesis submitted to the
School of Graduate Studies
in partial fulfilment of the
requirements for the degree of
Master of *Science*

Department of *Earth Sciences*
Memorial University of Newfoundland

April 2011

St. John's Newfoundland

Abstract

Travel time tomography calculations involving 3D velocity models have become more common place during the past decade or so. Numerous methods have been developed to solve the required forward modeling problem of boundary value ray tracing in 3D. For this problem, source and receiver positions are known and one or more time paths are sought between the fixed end points. Less attention has been given to the approach to model parametrization. Traditionally, the model has been subdivided into constant velocity cells, a process known as voxellation or cellular partitioning. A new approach to model parametrization involving numerically constructing the boundary of a homogeneous subsurface geological feature is proposed here and an efficient method for tracing rays through this model is presented. The ray tracing problem is solved by obtaining the minimum travel time path from a fixed source to a fixed receiver, and its associated travel time, as the solution to a nonlinear optimization problem based on Fermat's principle. The inversion technique will be regulated by using the area, perimeter and the total distance from each vertex to the center of the numerically defined surface as measures of model structure.

Acknowledgements

First and foremost, I would like to thank Dr. Colin G. Farquharson for all of his guidance and support. Without the immeasurable aid that he eagerly provided this thesis would not have been possible. Secondly, I would like to thank Dr. Charles Hurich for his willingness to answer any questions that arose as my research progressed. Finally, I would like to thank The Special Scholarships for Students to Pursue Graduate Studies Related to Resource Development, Buchans Scholarship Fund of ASARCO Incorporated and The School of Graduate Studies F. A. Aldrich Fellowship for the funding they provided throughout the course of my graduate program.

Contents

List of Tables

List of Figures

Chapter 1

Introduction

The word *Tomography* is derived from the Greek "tomos" (section) and "graphein" (to write) and means a picture of a cross-section of an object. In practice, the term denotes determining the internal properties of an object from external measurments by using rays that have passed through the object (Sheriff & Geldart, 1995). X-ray tomography has been used for some time in medical examinations and non-destructive testing (Sheriff & Geldart, 1995). The computer assisted tomography (CAT-scan) technique uses a series of two-dimensional X-ray images taken around a single axis of rotation to generate a three-dimensional image of the inside of an abject (Sheriff & Geldart, 1995).

Seismic tomography involves systematically investigating subsurface zones by transmitting very large numbers of seismic rays through them (Kearey et al., 2002). The method borrowed its name from the medical technology used for imaging the internal organs of a human body. The seismic imaging method, however, was developed independently of the medical community, and in fact was originally called the "3D Inversion Method" in the seismological community until the early 1980s (Iyer & Hirahara, 1993). The first

seismic tomography result was reported at the 1974 Fall meeting of the American Geophysical Union (Iyer & Hirahara, 1993). The study investigated the subsurface structure beneath the San Andreas fault system. Within a few years, the method was being applied to data from around the world and has continued to develop rapidly up to the present day.

Seismic borehole tomography involves the measurement of travel times between two or more boreholes. Data is collected using one hole for the seismic source and measuring first-arrival times using strings of geophones (receivers) in the others. Travel times are collected at regular intervals all the way down the hole(s) for each shot position. A simple example is shown in Figure 1.1, where only a limited subset of ray paths is shown.

If the internal structure and physical properties of the Earth were known precisely, the magnitude of any particular geophysical measurement could be predicted uniquely. Thus, for example, it would be possible to predict the travel time of a seismic wave traveling through an anomalous subsurface ore deposit. In geophysical surveying the problem is the opposite of the above, namely, to deduce some aspect of the Earth's internal structure on the basis of geophysical measurments taken at (or near) the Earth's surface (Kearey et al., 2002). The former type of problem is known as a *direct* problem, the latter as an *inverse* problem. Direct problems are theoretically capable of an unambiguous solution but inverse problems suffer from an inherent non-uniqueness in the conclusions that can be drawn (Kearey et al., 2002).

The total travel times for each ray are directly influenced by the structural

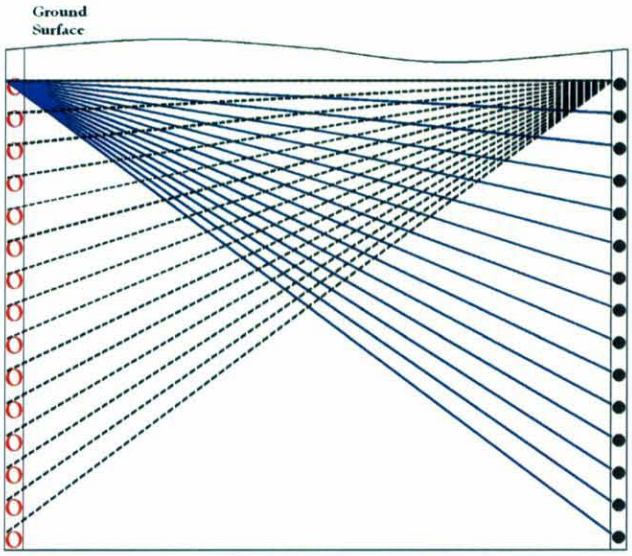

Figure 1.1: Idealized observation scheme for a simple borehole seismic transmission tomography survey. Black dots mark receivers, red circles mark sources. For clarity, only the ray paths from one source to all receivers (solid blue lines), and all sources to one receiver (dashed black lines) are shown (After Kearey et al., 2002).

and physical properties (velocity in particular) of the rocks being investigated and are the basic data used for interpretation. It is possible to turn these measurements on their heads, that is, invert them, and extract information about rock properties between boreholes. The resulting inversion produces a velocity model, enabling the identification of anomalous velocity zones lying between boreholes.

The information derived from seismic tomography may be used to predict

spatial variations in lithology, pore fluids, or rock fracturing, and the method is therefore of potential in a wide range of exploration and engineering applications (Kearey et al., 2002). As with many geophysical methods, it can also be applied on a variety of spatial scales, from ranges of hundreds of metres, down to engineering or archaeological investigations of single columns in ancient buildings (Cardarelli & Nardis, 2001). In this thesis, seismic borehole tomography will be used to investigate a synthetic scenario involving subsurface volcanogenic massive sulphide (VMS) ore deposits.

An important feature to any travel time inversion method is its approach to model parametrization. The standard approach to model parametrization involves dividing up the medium between boreholes into cells, a process known as voxellation or cellular partitioning (Sheriff & Geldart, 1995)(Figure 1.2). Each cell is assigned an initial seismic velocity and the time spent by each ray in each cell is calculated. The velocity assigned to each individual cell can be adjusted so that the errors between the observed travel times and the calculated ones are minimized. Although generally the number of observations is much larger than the number of cells and the problem is over determined, some cells may not have been traversed, so that their slowness cannot be determined and many of the travel paths may have traversed the same subset of cells so that their individual contributions cannot be separated (Sheriff & Geldart, 1995). These factors lead to the "smearing" of the resulting velocity model.

In order to rectify the issues associated with cellular partitioning, we

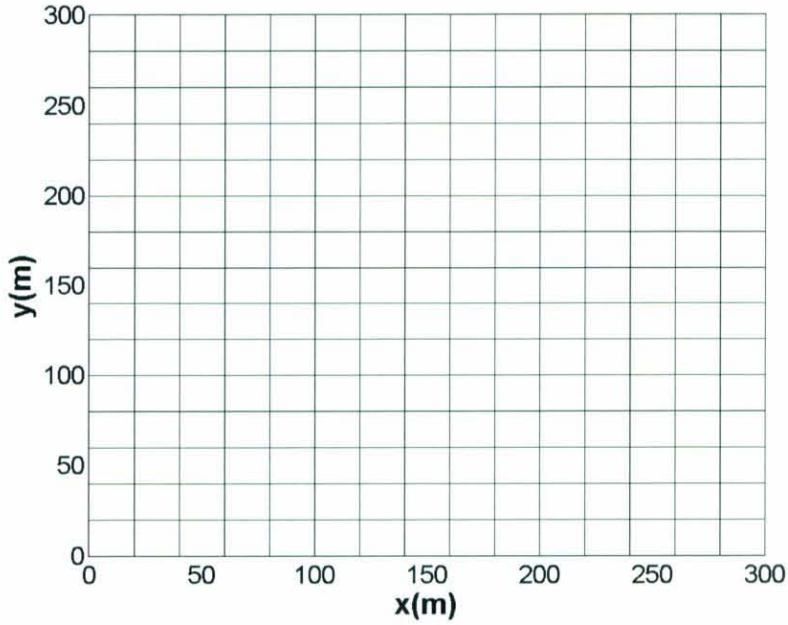

Figure 1.2: Subsurface mesh consisting of 225 20m x 20m squares.

propose to parametrize a model via a numerically defined surface consisting of a collection of line segments in 2D and triangular facets in 3D (Figure 1.3). The position of each line segment is defined by two vertices and each triangular facet by three. In both cases, the overall shape of the model can be changed by manipulating the position of these vertices. In 3D, each vertex is shared by multiple facets and each facet edge is shared by two facets. The surface is therefore closed and continuous.

Seismic ray tracing from a source to a receiver is a classic seismological problem. In order to solve both the forward and inverse borehole tomography problems in both 2D and 3D, the computation of ray paths and travel times

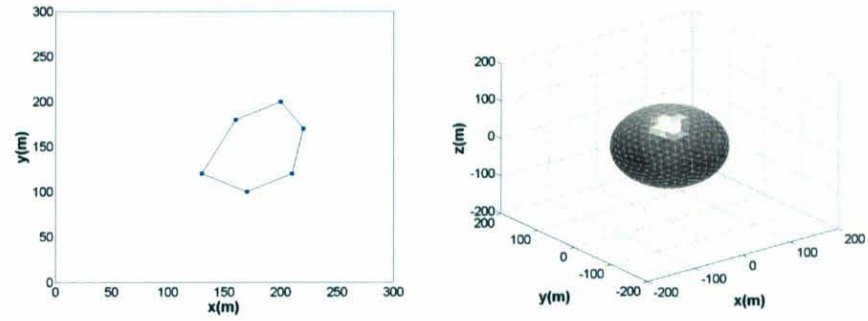

Figure 1.3: Examples of numerically defined surfaces in both 2D and 3D. *Left:* General 2D model defined by a collection of line segments. Each line segment is defined by two vertices (blue) *Right:* Tessellated sphere (radius=100m) containing 1280 triangles

are required as a first step. Traditionally, the problem of tracing rays has been posed as a system of first order differential equations or a two point boundary value problem (Jacob, 1970; Wesson, 1971; Pereyra et al., 1980). In "shooting" methods of raytracing, a fan of rays is shot from one point in the direction of the other. The correct path and travel time to connect the two points may be approached with successivly more accurate guesses. Such solutions for two- and three-dimensional media were derived more than 10 years ago (Gubbins & Julian, 1977). "Bending" methods of raytracing dissussed by Thurber (1987) start with an initial, most likely incorrect guess for the ray path. The ray path is subsquently bent by a perturbation method until it satisfies a minimum travel time criterion.

Transit times for seismic waves have been calculated in a variety of ways. Generally, more complicated media require more expensive and tricky schemes to find the transit times. Vidale (1988) presents a finite-difference

calculation of travel times. The travel times of the first arriving seismic waves through any velocity structure are rapidy computed on a two- or three-dimensional numerical grid by finite-difference extrapolation from point to point. Although this method is attractive, it is counter-productive since we are trying to avoid the traditional method of cellular partitioning.

In the last few decades, the ray tracing problem has also been solved via optimization using Fermat's principle, which consists of finding the minimum travel time ray path between source and receiver. Different optimization techniques have been used with varying degrees of success. Specifically, Chander (1975) approximates the integral for the travel time by a sum and solves for the minimum time directly. This method is only able to contend with simple flat interfaces and can not be used to trace rays through more complicated curved surfaces. Also, Um & Thurber (1987) present a two point bending optimization method based on Fermat's principle. Convergence of this method has not yet been established. More recently, Mao & Stuart (1997) presented a two point ray tracing method based on Fermat's principle assuming a piecewise linear ray path. Convergence of this method is not always guaranteed.

Many of the methods of ray tracing introduced above will be discussed in detail, however, since the primary interest of this paper is model parametrization as it applies to the inversion procedure, we simplify both the forward and inverse problems by assuming a linear raypath from source to reciever.

To exemplify the inherent non-uniqueness of the inverse problem, consider

a traditional cellular subsurface model containing over 1000 cells. Throughout the course of an inversion, the velocity assigned to each cell is adjusted until the difference between the observed and calculated travel times are minimized. With such a large number of model parameters (namely the velocity in each cell), there will be many different velocity combinations that minimize the data and thus provide a solution to the inverse problem.

The issue of non-uniqueness can be dealt with by minimizing some measure of model structure in conjunction with data misfit, a method known as minimum structure inversion. Of equal importance, minimum-structure inversion procedures generally are robust and reliable.

Traditional implementations of minimum-structure inversion procedures use a sum-of-squares, or l_2, measure of model structure. This is because minimizing such a measure results in a linear system to be solved. However, the models produced typically have a smeared-out, fuzzy character. Farquharson (2008) introduces a modification of the typical minimum-structure inversion algorithm that generates blocky, piecewise constant earth models more consistent with our real or percieved knowledge of the subsurface. The modified algorithm uses l_1-type measures in the measure of model structure instead of the traditional sum-of-squares, or l_2, measure.

The purpose of the work presented here is to apply a minimum structure inversion to a model parametrized by a numerically defined surface. This surface is not fixed and its position will be manipulated throughout the course of the inversion. In order to prevent the surface from turning inside out, ap-

propriate measures of model structure will be choosen. These regularization parameters will include the perimeter, the area and the sum of the distances from each vertex to the models' center. The resulting inversion will be compared to both an l_2 and non-l_2 minimum structure inversion of a traditional voxellated model.

The thesis will demonstrate that an inversion for a sharpe-edged, constant anomaly does a better job recovering synthetic data from a sharp, uniform subsurface feature than a minimum-structure tomographic approach. The synthetic data is consistent with the actual geology of an ore deposit. No test of the reverse situation has been attempted, namely, inverting data generated from a feature with a smoothly varying velocity assuming a defined shape. The resulting algorithm is intended to provide geophysicists with a more geology-specific inversion tool that out-performs its tradiational counterparts.

Chapter 2 begins with a discussion on the traditional l_2-type voxellation method. The forward and inverse problems are outlined and numerous examples are presented. The following chapter deals with voxellation using l_1-type measures. Chapter 4 introduces 2D numerically defined surfaces, discussing in detail the forward and inverse problems. Numerous examples are shown and these are compared to the traditional cellular approaches to model parametrization previously discussed. The next chapter follows from the previous by outlining numerically defined surfaces in 3D. Finally, the thesis ends with Chapter 6, which provides an overview of the research presented.

Chapter 2

2D Voxellation (l_2-type measure)

2.1 The Forward Problem

The seismic ray method is applicable to high frequency seismic body waves propagating in complex varying velocity structures (Červaný, 2001). Raytracing is based on the approximation that seismic energy of infinitely high frequency travels from source to receiver following a trajectory determined by the raytracing equations (Vidale, 1988). Physically, these equations describe how energy continues in the same direction until it is refracted by velocity variations. Modeling the energy propagation through a medium by ray tracing can be done by solving these equations, which are related to the velocity model, a set of reflecting or refracting boundaries and source/receiver pairs (Aki & Richards, 1980).

As discussed in the Introduction, the primary interest of this thesis is model parametrization as it applies to the inversion procedure. Therefore, in this chapter both the forward and inverse problems are simplified by assuming a straight raypath from source to reciever. Under the straight ray approximation, all directional changes attributed to velocity variations are

ignored. The forward problem for striaght ray tomography can be written generally as:

$$\mathbf{d}^{prod} = \mathbf{Lm} \tag{2.1}$$

where $\mathbf{d}^{prod}$ are the travel times, $\mathbf{L}$ is a matrix containing the distances traveled by each ray and $\mathbf{m}$ corresponds to the slowness value (i.e the reciprocal of the velocity) in each cell, which will be the model parameters sought in the inversion. Matrix $\mathbf{L}$ can be written generally as:

$$\mathbf{L} = \begin{pmatrix} l_{11} & l_{12} & \dots \\ l_{21} & l_{22} & \dots \\ \vdots & \vdots & \vdots \end{pmatrix} \tag{2.2}$$

Each row of the matrix $\mathbf{L}$ corresponds to a single ray and each column to a velocity layer.

Figure 2.1 shows the resultant ray paths through a 2500 m/s subsurface square for a mesh consisting of 225 20m by 20m cells. Sources are shown in red and receivers in green. There are 3 sources and 15 receivers providing 45 rays in total. The source and receiver configurations shown will be used for all the following examples involving a mesh of this size. When interpreting the results in subsquent sections, rays are numbered according to source from top to bottom along the y-axis. First, the intersection points between all rays and gridlines were calculated. Then the distance corresponding to each cell was determined and subsequently multiplied by the appropriate velocity in

order to determine the travel-time for each ray (See Appendix A).

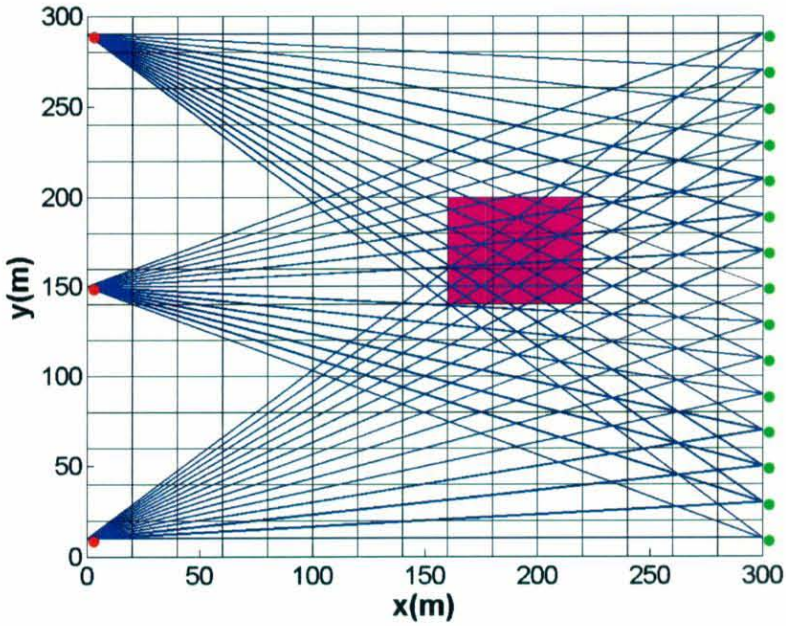

Figure 2.1: Resultant ray paths for a mesh consisting of 225 20m x 20m cells. The sources are shown in red and the receivers in green. *Magenta* corresponds to a velocity of 2500 m/s while *white* to 2000 m/s.

Figure 2.2 shows the resultant ray paths through a 2500m/s subsurface square for a mesh consisting of 3600 5m by 5m cells. Increasing the number of cells results in finer discretization and a more flexible model of the subsurface. Sources are shown in red and receivers in green. There is one extra receiver for the 3600 cell mesh and so one extra ray for each of the three sources. The reason for this is logistical, namely, to keep sources and recievers evenly spaced while making sure no ray overlaps with any of the horizontal grid lines. The source and receiver configurations shown will be used for all the

following examples involving a mesh of this size. The forward problem was calculated in the same manner as the mesh consisting of 225 cells discussed above (See Appendix A).

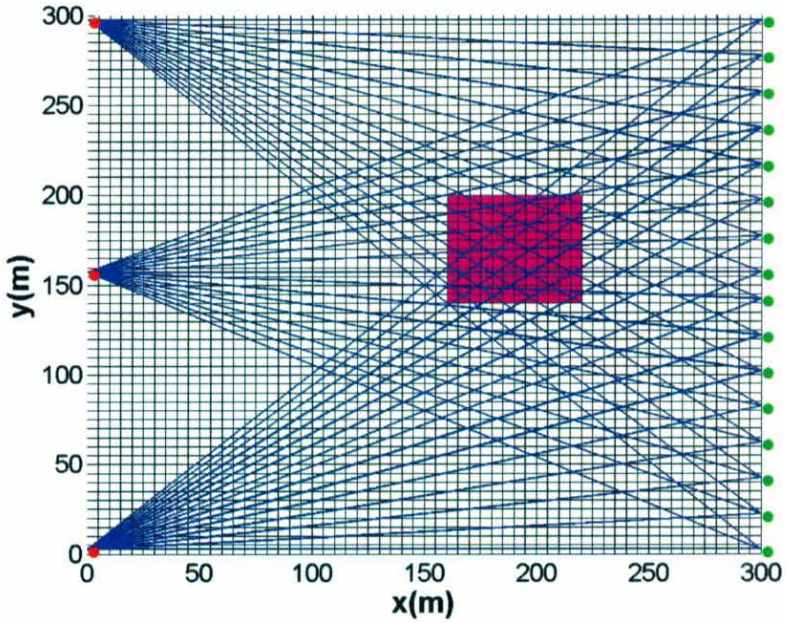

Figure 2.2: Resultant ray paths for a mesh consisting of 3600 5m x 5m cells. The sources are shown in red and the receivers in green. *Magenta* corresponds to a velocity of 2500 m/s while *white* to 2000 m/s.

All of the examples presented thus far involve velocity contrasts of 500 m/s. This is a typical velocity contrast exhibited by most ore deposits (Nolet, 1987). In situations where larger velocity contrasts exist (i.e. 3000 m/s), raypaths would bend and concentrate in high velocity areas and the straight ray approximation would therefore be inaccurate (Sheriff & Geldart, 1995).

2.2 The Inverse Problem

2.2.1 Newton's Method

In mathematics, Newton's method is a well-known algorithm for finding roots of equations. It can also be used to find stationary points (such as local maxima and minima) of functions, as such points are the roots of the derivative function (Bonnans et al., 2006).

We shall define a sequence x_n with a known initial guess x_0. The hope is that the sequence limits towards x_* which satisfies $f'(x_*) = 0$ (Bonnans et al., 2006).

The second order Taylor expansion of $f(x)$ at x_n is given by

$$f(x_n + \Delta x) = f(x_n) + f'(x_n)\Delta x + \frac{1}{2}f''(x_n)\Delta x^2 \tag{2.3}$$

where

$$\Delta x = x_{n+1} - x_n. \tag{2.4}$$

Equation 2.3 attains its extremum when Δx solves the linear equation:

$$f'(x) + f''(x)\Delta x = 0. \tag{2.5}$$

The sequence x_n is given by

$$x_{n+1} = x_n - \frac{f'(x_n)}{f''(x_n)} \tag{2.6}$$

where $n = 0, 1, \ldots n$. Equation 2.6 will converge towards the root of f (i.e. x_* for which $f(x_*)$=0) (Bonnans et al., 2006).

Equation 2.6 is valid provided the $f(x)$ is a twice-differentiable function well approximated by its second order Taylor expansion and the initial guess x_0 is chosen close enough to x_*.

The above iterative scheme can be generalized to several dimensions by replacing the derivative with the gradient, $\nabla f(x)$, and the reciprocal of the second derivative with the inverse of the Hessian matrix, **H** (Bonnans et al., 2006). The Hessian matrix, **H**, is the square matrix of second-order partial derivatives of a function (i.e. it describes the local curvature of a function of many variables) (Bonnans et al., 2006).

Given the real-valued function $f(x_1, x_2, \ldots, x_n)$, the gradient of f is given by

$$\mathbf{g} = \nabla f(x) = \left(\frac{\partial f}{\partial x_1} \cdots , \frac{\partial f}{\partial x_n} \right) \tag{2.7}$$

If all the second partial derivatives of f exist, then the Hessian matrix of f is the matrix

$$\mathbf{H} = \begin{pmatrix} \frac{\partial^2 f}{\partial x_1^2} & \frac{\partial^2 f}{\partial x_1 x_2} & \cdots & \frac{\partial^2 f}{\partial x_1 x_n} \\ \frac{\partial^2 f}{\partial x_2 x_1} & \frac{\partial^2 f}{\partial x_2^2} & \cdots & \frac{\partial^2 f}{\partial x_2 x_n} \\ \vdots & \vdots & \ddots & \vdots \\ \frac{\partial^2 f}{\partial x_n x_1} & \frac{\partial^2 f}{\partial x_n x_2} & \cdots & \frac{\partial^2 f}{\partial x_n^2} \end{pmatrix} \tag{2.8}$$

Taking the above into consideration, one obtains the iterative scheme

$$\mathbf{x}_{n+1} = \mathbf{x}_n - [\mathbf{H}]^{-1}\mathbf{g}, \tag{2.9}$$

where n≥0. Usually Newton's method is modified to include a small step size $\alpha > 0$ instead of $\alpha = 1$ (Bonnans et al., 2006),

$$\mathbf{x}_{n+1} = \mathbf{x}_n - \alpha[\mathbf{H}]^{-1}\mathbf{g}. \tag{2.10}$$

The step length helps control how large a "jump" the algorithm takes towards the minimum.

2.2.2 Gauss-Newton Algorithm

The Gauss-Newton algorithm is a method used to solve non-linear least squares problems (Fletcher, 1987). It can be seen as a modification of Newton's method for finding a minimum of a function. Unlike Newton's method, the Gauss-Newton algorithm can only be used to minimize a sum of squares function, but it has the advantage that second derivatives, which can be challenging to compute, are not required (Fletcher, 1987).

In what follows, the Gauss-Newton algorithm will be derived from Newton's method for function optimization via an approximation.

The recurrence relation for Newton's method for minimizing a function s of model parameters (i.e. the velocity in each cell), $\mathbf{m}$, is

$$\mathbf{m}^{s+1} = \mathbf{m}^s - \mathbf{H}^{-1}\mathbf{g} \tag{2.11}$$

where $\mathbf{g}$ denotes the gradient vector of s and $\mathbf{H}$ denotes the Hessian matrix of s (Nocedal & Wright, 1999).

A measure of the misfit between the predicted ($\mathbf{d}^{prd}$) and observed ($\mathbf{d}^{obs}$) travel times is given by:

$$s(\mathbf{m}) = \sum_{i=1}^{m} (d_i^{prd} - d_i^{obs})^2 \tag{2.12}$$

Taking $r_i = (d_i^{obs} - d_i^{prod})$, Equation 2.12 can be rewritten more compactly as

$$s(\mathbf{m}) = \sum_{i=1}^{m} r_i^2(\mathbf{m}) \tag{2.13}$$

The gradient can be written as

$$g_j = 2\sum_{i=1}^{m} \frac{\partial r_i}{\partial m_j}. \tag{2.14}$$

Elements of the Hessian are calculated by differentiating the gradient elements, g_j, with respect to m_k.

$$H_{jk} = 2\sum_{i=1}^{m}\left(\frac{\partial r_i}{\partial m_j}\frac{\partial r_i}{\partial m_k} + r_i\frac{\partial^2 r_i}{\partial m_j \partial m_k}\right). \tag{2.15}$$

The Gauss-Newton method is obtained by ignoring the second-order derivative terms (the second term in Equation 2.15) (Nocedal & Wright, 1999). That is, the Hessian is approximated by

$$H_{jk} \approx 2\sum_{i=1}^{m} J_{ij}J_{ik} \tag{2.16}$$

where $J_{ij} = \frac{\partial r_i}{\partial m_j}$ are entries of the Jacobian, $\mathbf{J}_r$. The gradient and the approximate Hessian can be written in matrix notation as

$$\mathbf{g} = 2\mathbf{J}_r^T r,\ \mathbf{H} \approx 2\mathbf{J}_r^T\mathbf{J}_r \tag{2.17}$$

These expressions are substituted into the Equation 2.11 above to obtain the iterative solution to the inverse problem

$$\mathbf{m}^{s+1} = \mathbf{m}^s - \alpha(\mathbf{J}_r^T\mathbf{J}_r)^{-1}\mathbf{J}_r^T r. \tag{2.18}$$

2.2.3 Minimum Structure Inversion

The geophysical inverse problem with respect to cellular partitioning is non-unique both fundamentally and numerically due to the large number of model parameters (i.e. the number of cells). A larger number of cells means finer discretization and is needed in order to have a more flexible model. In order to

counter this ill-posedness, a measure of some property of the model structure is minimized in conjunction with the measure of data misfit. So find $\mathbf{m}$ which minimizes:

$$\Phi = \varphi_d + \lambda \varphi_m \tag{2.19}$$

where φ_d is a measure of the data misfit and is given by:

$$\varphi_d = \left\| \mathbf{W}_d (\mathbf{d}^{obs} - \mathbf{d}^{prd}) \right\|_2^2 \tag{2.20}$$

where $\mathbf{d}^{obs}$ is the vector of observations, $\mathbf{d}^{prd}$ is the vector of data computed for the vector $\mathbf{m}$ of model parameters, and $\mathbf{W}_d$ is a diagonal matrix whose elements are the reciprocals of the estimates of the standard deviations of the noise in the observations (Farquharson, 2008). Also, φ_m is a measure of model structure and is given by:

$$\varphi_m = \|\mathbf{W}_z \, \mathbf{m}\|_2^2 + \|\mathbf{W}_x \, \mathbf{m}\|_2^2 \tag{2.21}$$

$\mathbf{W}_x$ and $\mathbf{W}_z$ are given by:

$$\mathbf{W}_x = \begin{pmatrix} \frac{1}{\Delta x_1} & \frac{-1}{\Delta x_1} & 0 & 0 & \cdots \\ 0 & \frac{1}{\Delta x_2} & \frac{-1}{\Delta x_2} & 0 & \cdots \\ \vdots & \vdots & \vdots & \vdots & \vdots \end{pmatrix} \tag{2.22}$$

$$\mathbf{W}_z = \begin{pmatrix} \frac{1}{\Delta z_1} & 0 & 0 & \cdots & \frac{-1}{\Delta z_1} & 0 \\ 0 & \frac{1}{\Delta z_2} & 0 & 0 & \cdots & \frac{-1}{\Delta x_2} \\ \vdots & \vdots & \vdots & \vdots & \vdots & \vdots \end{pmatrix} \tag{2.23}$$

where Δx_n and Δz_n are the horizontal and vertical distances measured from the center of a cell to an adjacent one, repectively (Figure 2.3).

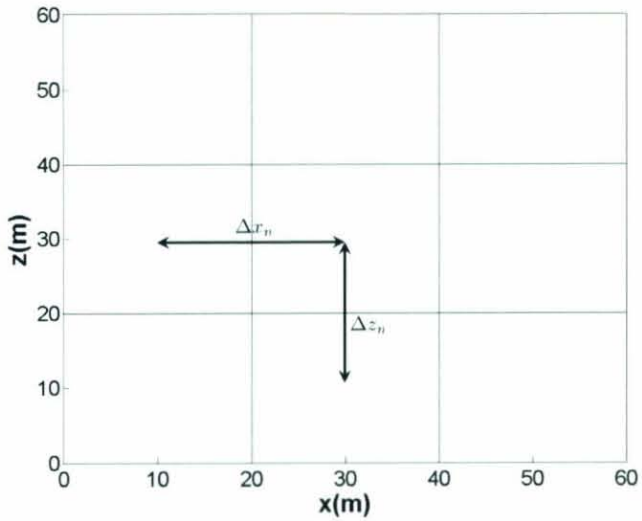

Figure 2.3: Schematic illustrating Δx_n and Δz_n.

The Gauss-Newton solution for $\delta\mathbf{m}$ at the n^{th} iteration is:

$$\begin{aligned} \left(\mathbf{J}^T\mathbf{W}_d^T\mathbf{W}_d\mathbf{J} + \lambda\left(\mathbf{W}_x^T\mathbf{W}_x + \mathbf{W}_z^T\mathbf{W}_z\right)\right)\delta\mathbf{m} = \\ \mathbf{J}^T\mathbf{W}_d^T\mathbf{W}_d\left(\mathbf{d}^{obs} - \mathbf{d}^{prd}\right) - \lambda\left(\mathbf{W}_x^T\mathbf{W}_x\mathbf{m}_n - \mathbf{W}_z^T\mathbf{W}_z\mathbf{m}_n\right) \end{aligned} \tag{2.24}$$

where λ is the trade-off parameter, which regulates the "strength" afforded

to the measure of model structure. λ is varied to get the appropriate misfit. The inverse problem in this case is linear and only one iteration of Equation 2.24 is required to obtain a result.

As discussed above, the Jacobian, J_{ij}, is given by

$$\frac{\partial(d_i^{prd} - d_i^{obs})}{\partial m_j} = \frac{\partial r_i}{\partial m_j} \tag{2.25}$$

where $\mathbf{d}^{prd}$ and $\mathbf{d}^{obs}$ are the predicted and observed travel-times, respectively. According to Equation 2.25, the Jacobian can be described as a change in travel-time with respect to the change in model parameters. In this case, the model parameters are the slowness values of each cell. For the straight-ray case, the Jacobian is therefore equivalent to the matrix $\mathbf{L}$ in Equation 2.2 containing the distances traveled by each ray (See Appendix A).

2.3 Results

As a note, Gaussian random noise of standard deviation equal in magnitude to 1% of a datum was added to create all the data sets used throughout this thesis.

The synthetic travel time obtained from a 2500m/s subsurface square was inverted using a mesh consisting of 225 20m x 20m cells (Figure 2.4). In order to determine the quality of the data misfit, the values in Figure 2.4 (c) need to be compared to the corresponding noise values. Presumably, a good fit means most of these values fall within +/- 1% of the datum

at each point. For example, take the first point in Figure 2.4 (c). The observed travel-time for this ray is 0.205s. Therefore, $t_{calc} - t_{syn}$ should fall between +/- 0.00205s. This is indeed the case as all the values in Figure 2.4 (c) are 4 orders of magnitude smaller than this range. It can then be stated that the synthetic and resultant travel-times correspond very well. The background velocity obtained from the inversion also matches quite well with its synthetic counterpart. However, although the general position of the anomaly is correct, it is "smeared" along the raypaths and its velocity is too low. A rescaled version using the maximum and minimum calculated velocities is shown in Figure 2.5.

In order to model more complex (and realistic) subsurface structures, additional cells are needed. The synthetic travel-time for the same 2500m/s subsurface square was inverted using a mesh consisting of 3600 5m x 5m cells (Figure 2.6). Both the synthetic and resultant travel times correspond very well. The background velocity obtained from the inversion also matches quite well with its synthetic counterpart. Just as with the previous example, the general location of the deposit is correct but it is "smeared" along the raypaths and its velocity is too low. A rescaled version using the maximum and minimum calculated velocities is shown in Figure 2.7. Using a greater number of cells is advantageous in that it provides more detail and thus better represents more complex subsurface structures.

One purpose of this research is to compare the traditional cellular approach to inversion with that of a numerically defined surface. Figure 2.8

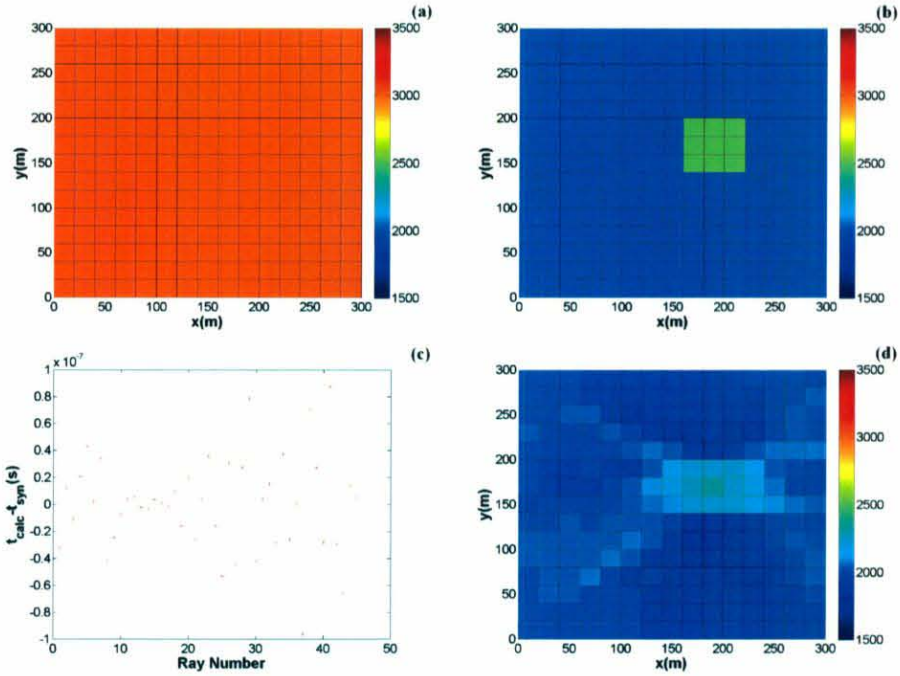

Figure 2.4: Minimum structure inversion (l_2-type measure) result for a 2500m/s subsurface square using a mesh of 225 20m x 20m cells: (a) Initial input velocity model. (b) True velocity model. (c) Difference between calculated (i.e. inverted) travel-time and synthetic travel-time. (d) Resultant velocity model.

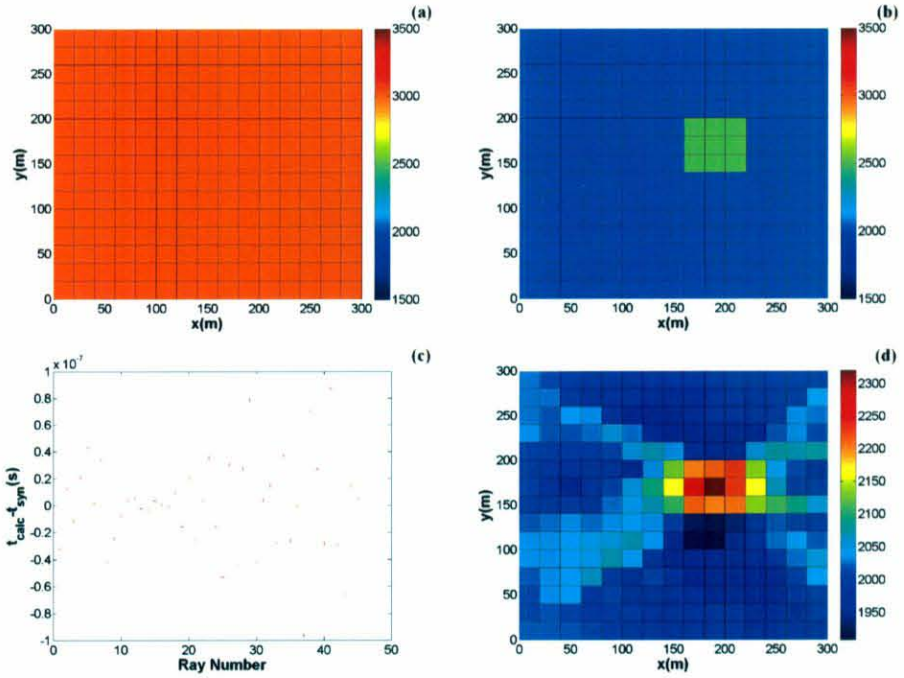

Figure 2.5: Rescaled minimum structure inversion (l_2-type measure) result for a 2500m/s subsurface square using a mesh of 225 20m x 20m cells: (a) Initial input velocity model. (b) True velocity model. (c) Difference between calculated (i.e. inverted) travel-time and synthetic travel-time. (d) Rescaled resultant velocity model.

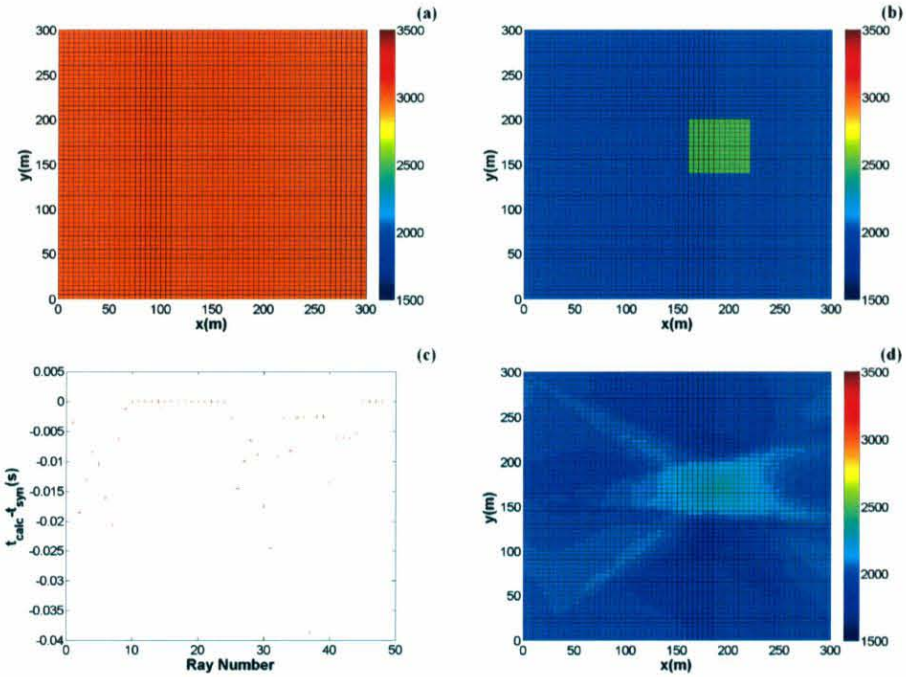

Figure 2.6: Minimum structure inversion (l_2-type measure) result for a 2500m/s subsurface square using a mesh of 3600 5m x 5m cells: (a) Initial input velocity model. (b) Synthetic velocity model. (c) Difference between calculated (i.e. inverted) travel-time and synthetic travel-time. (d) Resultant velocity model.

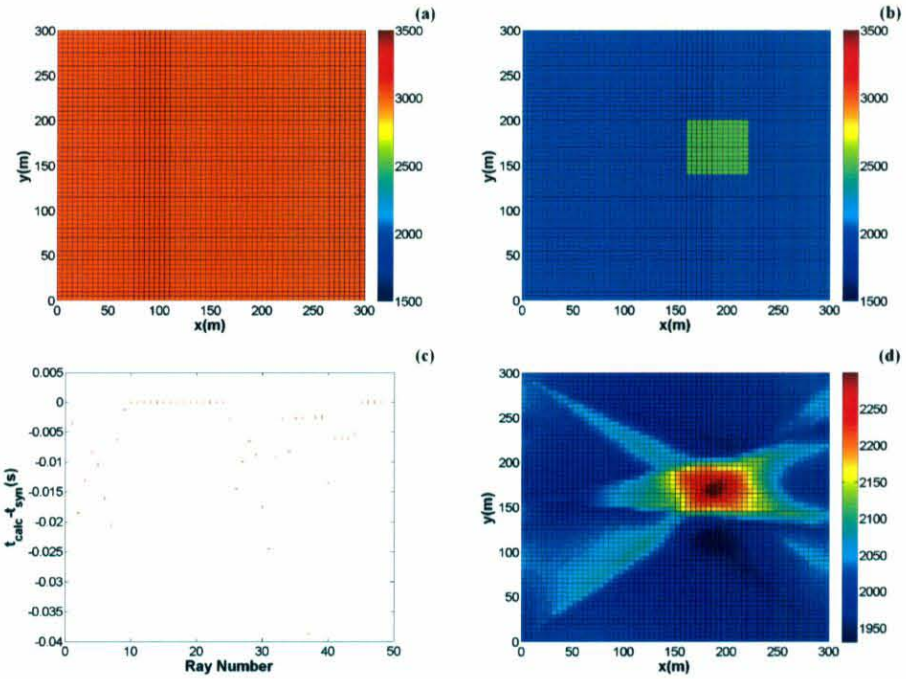

Figure 2.7: Rescaled minimum structure inversion (l_2-type measure) result for a 2500m/s subsurface square using a mesh of 3600 5m x 5m cells: (a) Initial input velocity model. (b) Synthetic velocity model. (c) Difference between calculated (i.e. inverted) travel-time and synthetic travel-time. (d) Rescaled resultant velocity model.

shows the inversion results for a 2500m/s kidney-bean shaped subsurface structure defined by twenty line segments, which will be used as a synthetic velocity model in subsequent sections. Both the synthetic and resultant travel times correspond fairly well. The background velocity obtained from the inversion also matches quite well with its synthetic counterpart. Just as with the previous example, the general location of the deposit is correct but it is "smeared". The velocity of the deposit in this instance is again too low. A rescaled version using the maximum and minimum calculated velocities is shown in Figure 2.9.

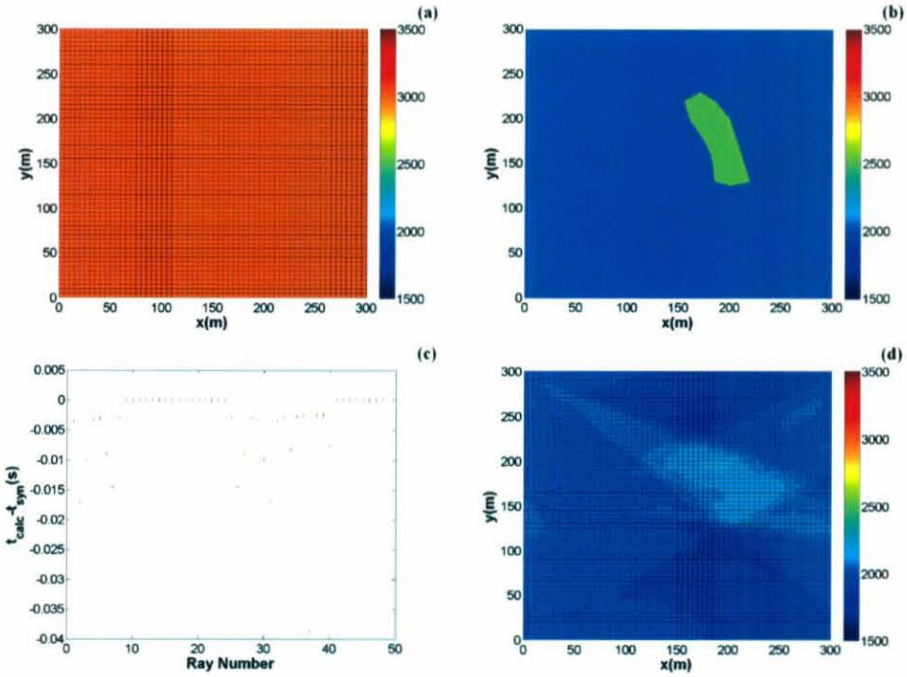

Figure 2.8: Minimum structure inversion (l_2-type measure) result for a 2D numerically defined shape using a mesh of 3600 5m x 5m cells: (a) Initial input velocity model. (b) Synthetic velocity model. (c) Difference between calculated (i.e. inverted) travel-time and synthetic travel-time. (d) Resultant velocity model.

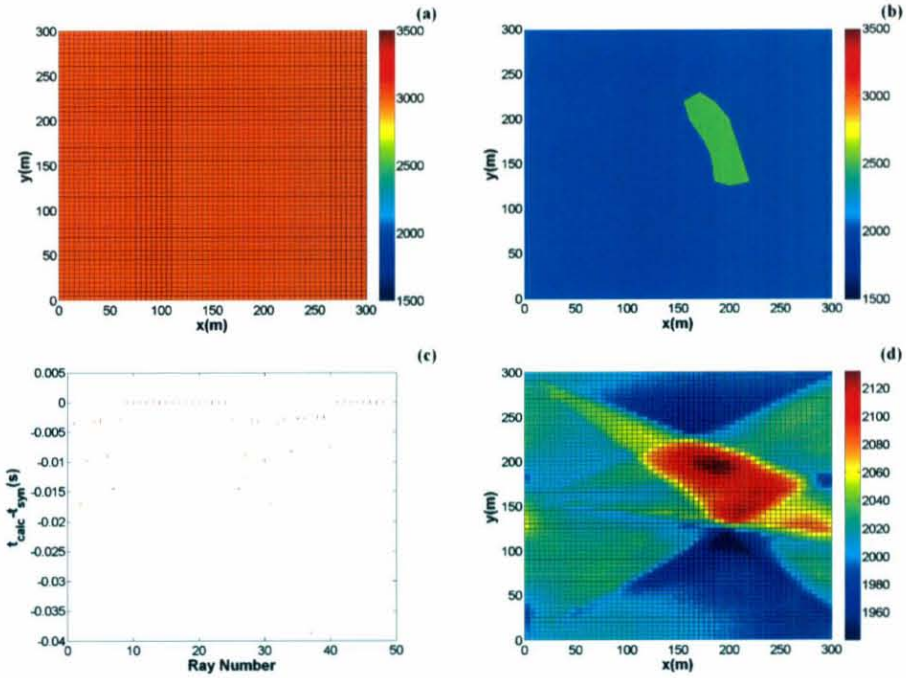

Figure 2.9: Rescaled minimum structure inversion (l_2-type measure) result for a 2D numerically defined shape using a mesh of 3600 5m x 5m cells: (a) Initial input velocity model. (b) Synthetic velocity model. (c) Difference between calculated (i.e. inverted) travel-time and synthetic travel-time. (d) Rescaled resultant velocity model.

Chapter 3

2D Voxellation(l_1-type measure)

3.1 The Inverse Problem

The typical minimum structure inversion can be modified so that it generates more blocky, piecewise constant Earth models as opposed to fuzzy, smeared-out ones (Farquharson, 2008). The modified algorithm uses l_1-type measures in the measure of model structure instead of the sum-of-squares, or l_2, measure (Farquharson, 2008). The measure of the amount of structure in the model, φ_m, has the form

$$\varphi_m = \sum_k \alpha_k \varphi_k(v_k) \tag{3.1}$$

where

$$v_k = \mathbf{W}_k(\mathbf{m} - \mathbf{m}_k^{ref}) \tag{3.2}$$

k will vary over x and y.

A general form for φ_d and φ_k is

$$\varphi(x) = \sum_j \rho(x_j) \tag{3.3}$$

where x_j are the elements of the vector $\mathbf{x}$, which will be $\mathbf{v}_k$ from above, and the summation is over all elements in the vector (Farquharson, 2008). There are numerous possibilities for the specific form of the measure. I choose to use

$$\rho(x) = (x^2 + \epsilon^2)^{p/2-1} \tag{3.4}$$

where ϵ is a small number and p is 1 in order to achieve an l_1 norm.

To minimize Φ, Equation 2.19 is differentiated with respect to the perturbations of the model parameters, and the resulting derivatives are equated to zero (Farquharson, 2008). Differentiating the general form of the measures (Equation 3.3) gives

$$\frac{\partial \varphi(x)}{\partial \delta m_k} = \sum_j \rho'(x_j) \frac{\partial x_j}{\partial \delta m_k}, \tag{3.5}$$

that is,

$$\frac{\partial \varphi(x)}{\partial \delta m} = \mathbf{B}^T \mathbf{q}, \tag{3.6}$$

where $\partial\varphi/\partial\delta m = (\partial\varphi/\partial\delta m_1, \cdots, \partial\varphi/\partial\delta m_N)^T$, $B_{ij} = \partial x_i/\partial\delta m_j$, and $\mathbf{q} = (\rho'(x_1), \cdots, \rho'(x_N))^T$. Equation 3.6 can be reformulated by introducing a diagonal matrix:

$$\mathbf{R} = diag\{\rho'(x_1)/x_1, \cdots, \rho'(x_n)/x_n\}, \tag{3.7}$$

which leads to

$$\frac{\partial \varphi(x)}{\partial \delta m} = \mathbf{B}^T \mathbf{R} \mathbf{x}. \tag{3.8}$$

The elements of the matrix $\mathbf{R}$ are

$$R_{ii} = \rho(x_i^2 + \epsilon^2)^{p/2-1} \tag{3.9}$$

The linear system of equations to be solved at each iteration is therefore (Compare with Equation 2.24)

$$\begin{aligned}[\mathbf{J}^T \mathbf{W}_d^T \mathbf{R}_d \mathbf{W}_d \mathbf{J} + \beta^n \sum_k \alpha_k \mathbf{W}_k^t \mathbf{R}_k \mathbf{W}_k] \delta \mathbf{m} = \mathbf{J}^T \mathbf{W}_d^T \mathbf{R}_d \mathbf{W}_d (\mathbf{d}^{obs} \\ - \mathbf{d}^{n-1}) + \beta^n \sum_k \mathbf{W}_k^T \mathbf{R}_k \mathbf{W}_k (\mathbf{m}_k^{ref} - \mathbf{m}^{n-1}).\end{aligned} \tag{3.10}$$

The matricies $\mathbf{R}$, as well as the Jacobian matrix, depend on the model and are updated at each iteration (Farquharson, 2008) (See Appendix B).

3.2 Results

In all the examples presented in the previous chapter, the resultant velocity model appears fuzzy and smeared-out. To keep this from occuring, the

data from Figure 2.8 were inverted using the modified minimum structure algorithm involving l_1-type measures discussed in the previous section(Figure 3.1). The inversion generated a more blocky resultant velocity model that is more consistent with the synthetic velocity model. Additionally, the inverted velocities are no longer too low and instead correspond much better to the synthetic model. On the other hand, the resultant velocity model lacks the kidney bean shape of the synthetic model and also appears to be distorted in terms of dip and location along the direction of the raypaths.

Of note, the dip is somewhat affected by the nature of the measures themselves. That is, the l_1 ,measure favors vertical and horizontal dipping synthetic models (Farquharson, 2008).

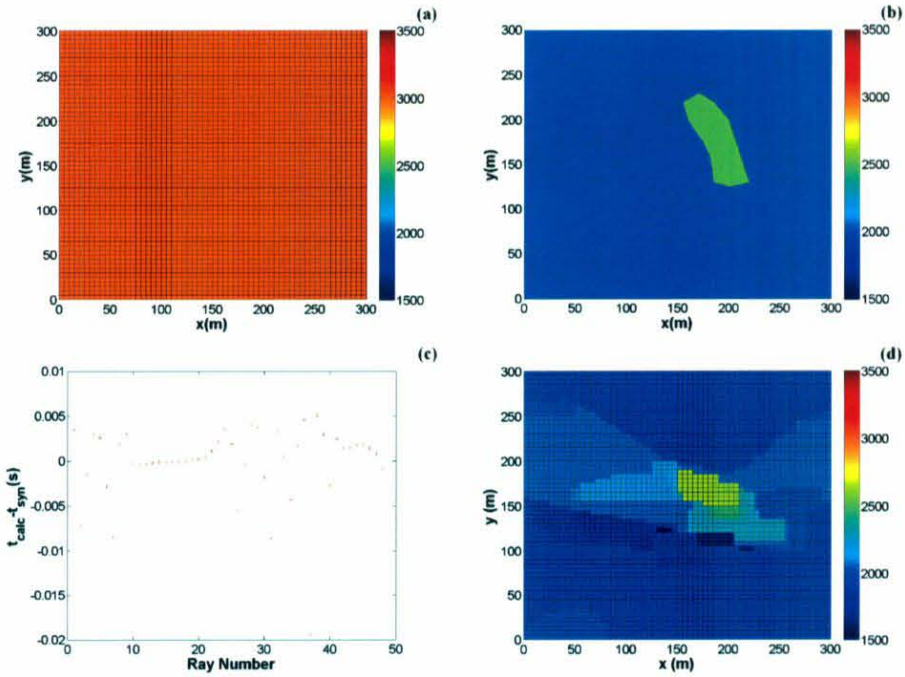

Figure 3.1: l_1 inversion result for a 2D numerically defined shape using a mesh of 3600 5m x 5m cells: (a) Initial input velocity model. (b) Synthetic velocity model. (c) Difference between calculated (i.e. inverted) travel-time and synthetic travel-time. (d) Resultant velocity model.

Chapter 4

Numerically Defined Surface (2D)

4.1 Model Parametrization

The proposed inversion technique involves constructing the boundary of a homogeneous (i.e., constant velocity) subsurface geological feature, embedded in a homogeneous host rock. I propose to parametrize a model in 2D via a collection of line segments, each of which is defined by two vertices (Figure 4.1). The position of each vertex will be manipulated to create different models. The position of all vertices and the velocities of both the deposit and host rock will be the model parameters sought in the inversion.

4.2 The Forward Problem

As discussed in the Introduction, the primary interest of this paper is model parametrization as it applies to the inversion procedure. Therefore, in this chapter, I again simplify both the forward and inverse problems by assuming a linear raypath from source to reciever. Under the straight ray approximation, all directional changes attributed to velocity variations are ignored.

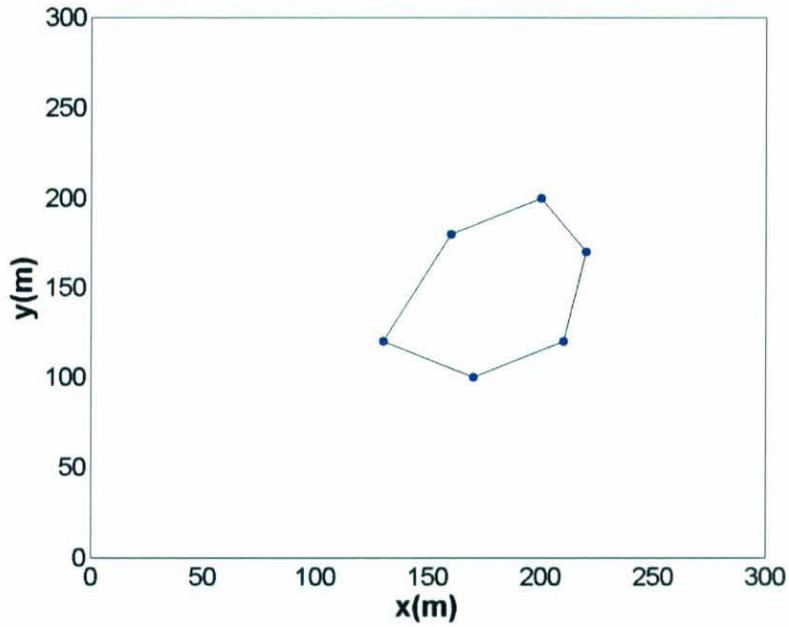

Figure 4.1: General 2D model defined by a collection of line segments. Each line segment is defined by two vertices (blue).

When defining a geological structure via a collection of line segments in 2D, seismic rays will only be traveling through a maximum of two interfaces. While it is possible that during the inversion procedure two segments could cross, effectively turning the model inside out, the forward solver will detect an extra intersection point and subsequently shut down.

Figure 4.2 shows the resultant ray paths through a 2500 m/s twenty-segment subsurface kidney-bean shaped structure. Sources are shown in red and recievers in green. There are 3 sources and 15 receivers providing 45 rays in total. The source and receiver configurations shown will be used for

all the following examples involving 2D numerically defined surfaces. When interpreting the results in subsquent sections, rays are numbered from top to bottom along the y-axis. The intersection points for each ray were calculated. The distances corresponding to the host rock and the deposit were determined and subsequently multiplied by the appropriate velocity in order to determine the travel time for each ray (See Appendix C).

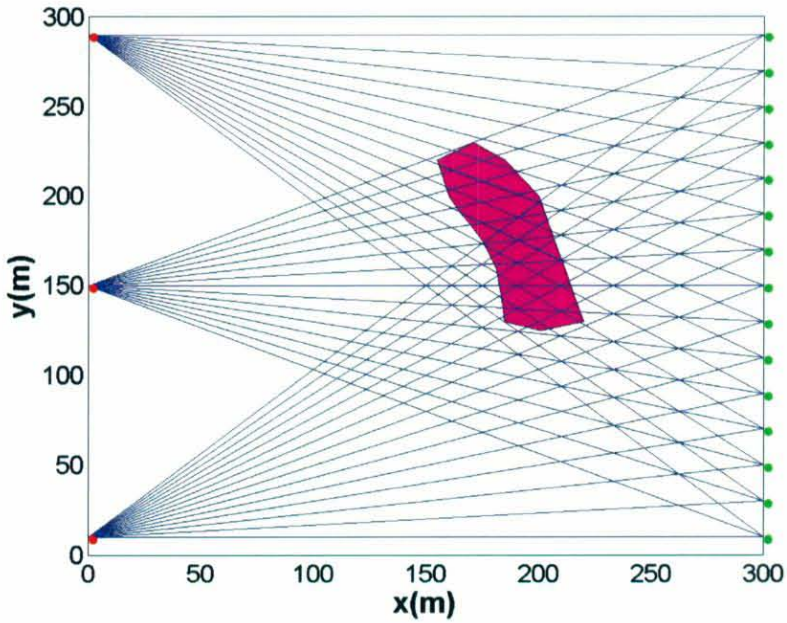

Figure 4.2: Resultant ray paths through a 2500m/s twenty-segment subsurface kidney-bean shaped structure. Sources are shown in red and receivers in green. *Magenta* corresponds to a velocity of 2500m/s while *white* to 2000m/s.

4.3 Minimization of Misfit Inversion

4.3.1 Theory

In certain instances, in particular when there are only a few model parameters, the geophysical inverse problem can be solved by a simple minimization of data misfit. This is the case in two dimensions when using only a few line segments to define a model. The inverse problem can be solved using the Gauss-Newton algorithm discussed previously (Equation 2.18) (See Appendix C). In this case the model parameters, **m**, being sought in the inversion are the x-y coordinates of each vertex and the velocity of the ore deposit and the host rock.

In order to calculate the Jacobian, rays are first traced through a velocity model and the subsquent travel-times are calculated. Next, each model parameter being sought is sequentially perturbed by a small amount and the travel-times are again calculated. The initial travel-times are then subtraced from these values and each result is divided by the appropriate perturbation factor giving the Jacobian matrix (See Appendix C). This method for calculating the Jacobian applies to all the following examples involving numerically defined surfaces and to avoid repitition wil not be discussed in detail again.

4.3.2 Results

Figure 4.3 shows the inversion of a six sided polygon using only the minimization of data misfit and no measure of model structure. The upper left panel shows the true model while the upper right is a picture of the starting model or initial 'guess' at the solution. The lower left panel is the resulting inversion and the right shows the difference between the calculated (i.e. inverted) travel-time and the synthetic travel-time. To the right of all models is a colorbar representing the velocity in m/s for that particular graph. The resultant velocity model corresponds well to its synthetic counterpart. Gaussian noise of standard deviation equal in magnitude to 1% of a datum was added to the synthetic data. The values of data misfit shown in Figure 4.3 (d) all fall within + 1% of the noise for each point. In fact, these values are two orders of magnitude smaller than the associated noise. This suggests a good fit between the observed and calculated travel-times.

The majority of the computation time is spent adjusting the background velocity of the model. Figure 4.4 shows the same inversion except that the background (or host rock) velocity is no longer a model parameter being sought but is instead known. As compared to Figure 4.3, the velocity of the deposit is more accurately depicted and the number of iterations is decreased by 110. While the kidney-bean shape is achieved, the resultant velocity model is not as "smooth" as in Figure 4.3.

Although the result presented in Figure 4.3 provides a good representation

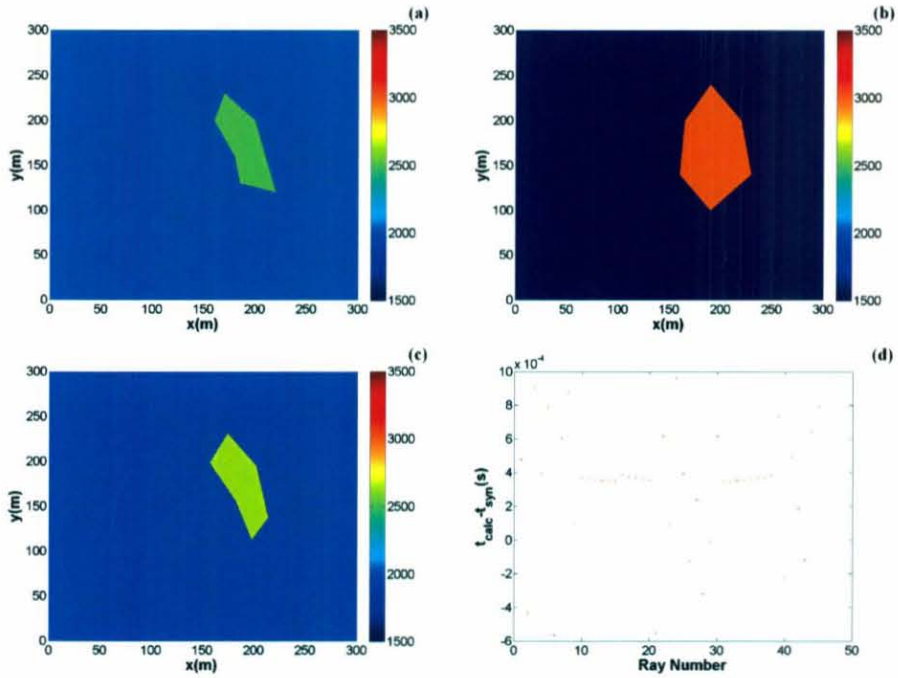

Figure 4.3: Two-dimensional minimization of misfit inversion results for a six segment model: (a) True velocity model. (b) Initial velocity model. (c) Resultant velocity model. (d) Difference between calculated (i.e. inverted) travel-time and synthetic travel-time.

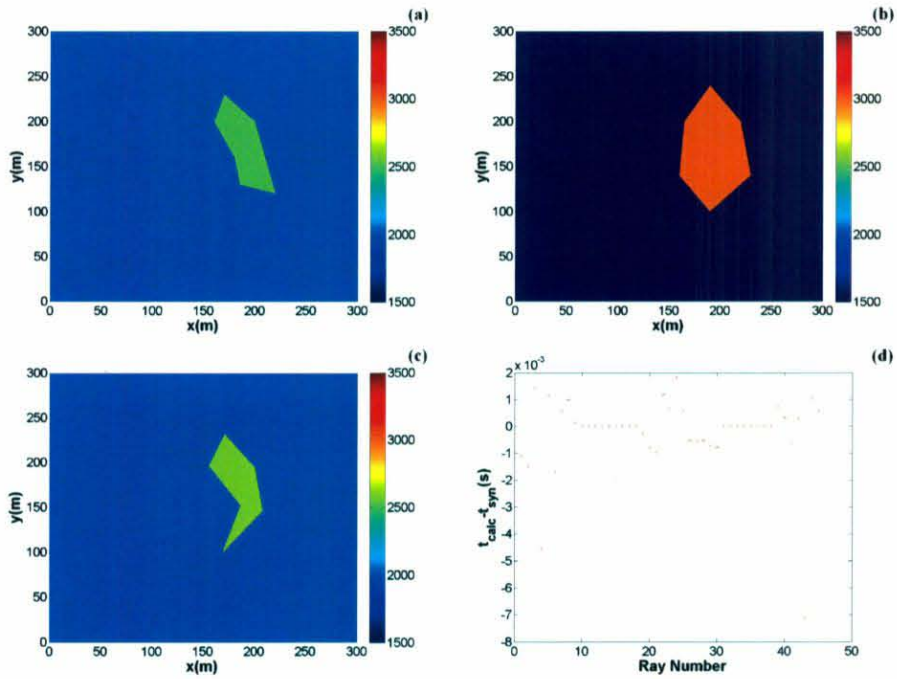

Figure 4.4: Two-dimensional minimization of misfit inversion results for a six segment model (background velocity known): (a) True velocity model. (b) Initial velocity model. (c) Resultant velocity model. (d) Difference between calculated (i.e. inverted) travel-time and synthetic travel-time.

of the true velocity model, the natural progression is to move towards more complex models which can, in principle, better represent the Earth's real subsurface. To do this, additional verticies must be inserted. Figure 4.5 shows results for the same inversion as the first above, but with the model now consisting of ten sides as opposed to the 6 in the first example (See Appendix D). Also, the upper right panel has been replaced by a trace of the change in perimeter of the resultant velocity model. Figure 4.6 shows the associated starting velocity model.

As can be seen from Figure 4.5, the perimeter of the resultant velocity model is ill-behaved and the inversion process subsequently shuts down after only 18 iterations. Specifying the background velocity and removing it from the set of model parameters being sought does not improve the solution (Figure 4.7). In order to counteract this from occuring, we switch to a minimum structure type of inversion.

4.4 Minimum Structure Inversion of a Numerically Defined Surface Model

4.4.1 Measures of Model Structure

A total of three measures of model structure will be implemented. These include the perimeter and area of the numerically defined surface as well as the total distance from each vertex to the centroid. All three parameters will

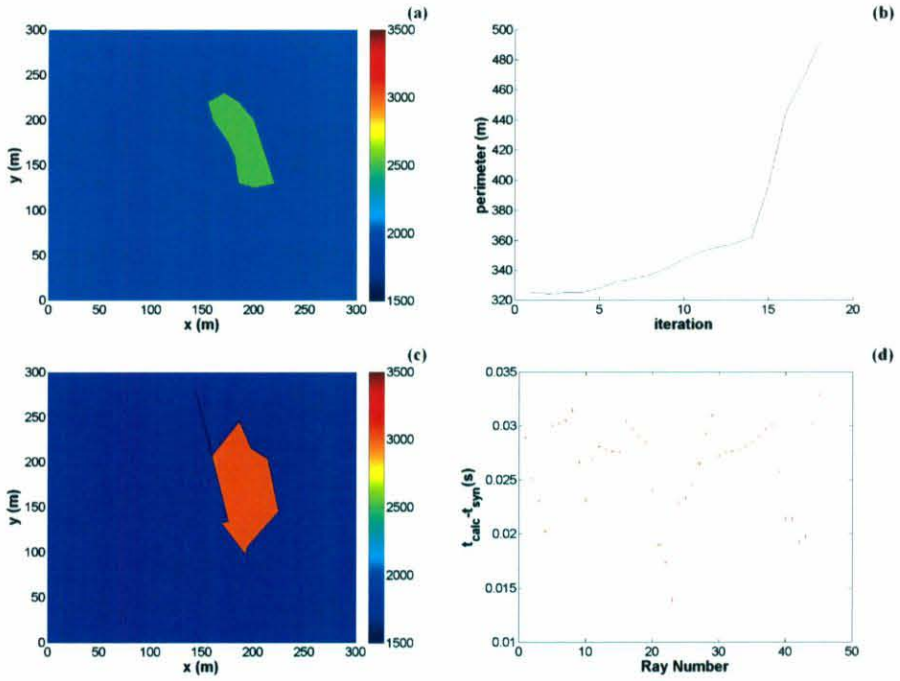

Figure 4.5: Two-dimensional minimization of misfit inversion results for a ten segment model: (a) True velocity model. (b) Resultant velocity model perimeter trace. (c) Resultant velocity model. (d) Difference between calculated (i.e. inverted) travel-time and synthetic travel-time.

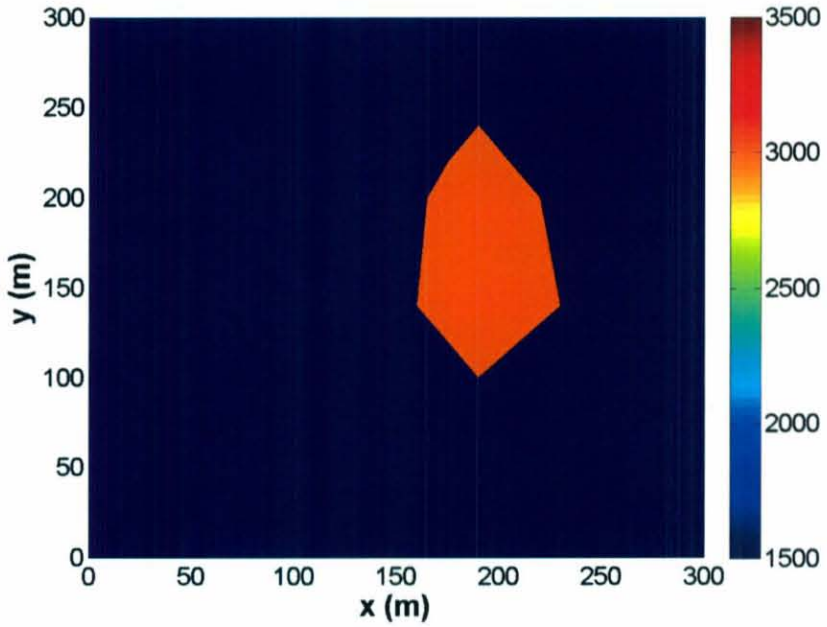

Figure 4.6: Initial velocity model for a ten segment 2D polygon.

be introduced and discussed sequentially below.

The most obvious initial choice for the measure of model structure to minimize is the perimeter, which is given by

$$P = \sum_{i=0}^{n-1}((x_{i+1} - x_i)^2 + (y_{i+1} - y_i)^2)^{\frac{1}{2}}. \tag{4.1}$$

To close the polygon, the first and last verticies are the same, i.e., $x_n, y_n = x_0, y_0$ (Figure 4.8).

Next, the area of a polygon is given by: (Burke, 1988)

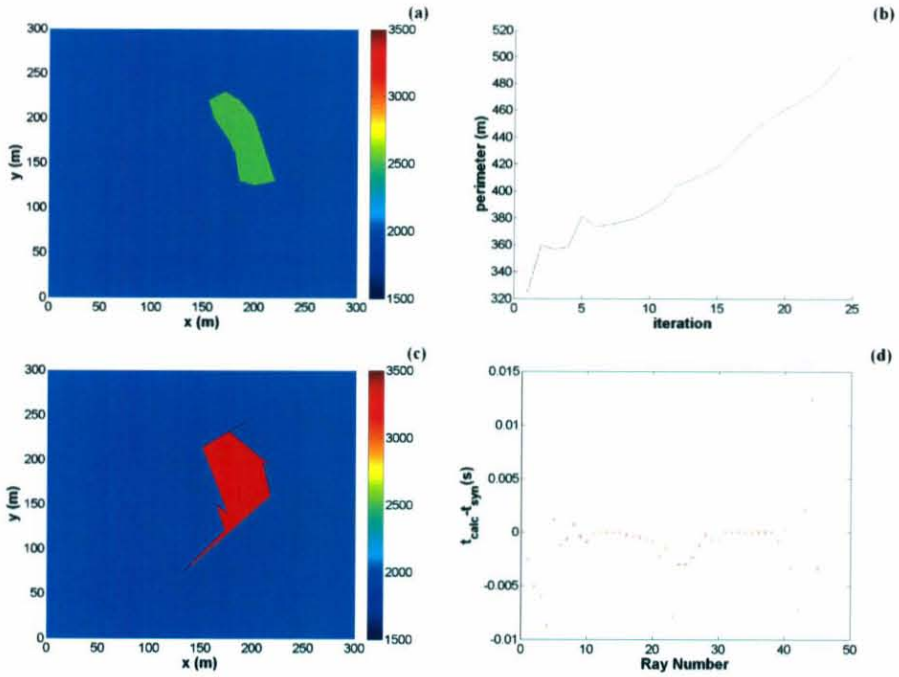

Figure 4.7: Two-dimensional minimization of misfit inversion results for a ten segment model (background velocity known): (a) True velocity model. (b) Resultant velocity model perimeter trace. (c) Resultant velocity model. (d) Difference between calculated (i.e. inverted) travel-time and synthetic travel-time.

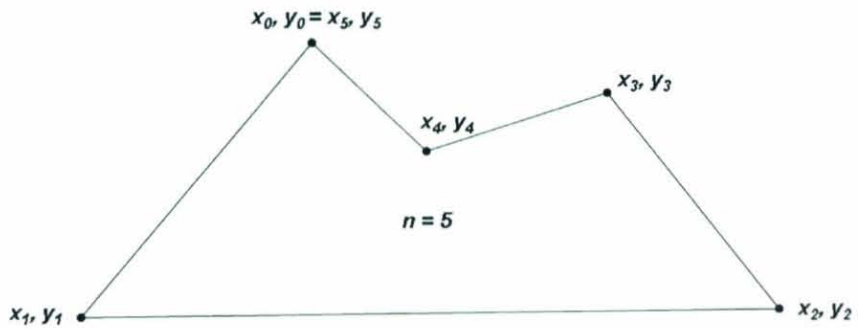

Figure 4.8: Schematic of a two-dimensional polygon.

$$A = \frac{1}{2}\sum_{i=0}^{n-1}(x_i y_{i+1} - x_{i+1} y_i). \tag{4.2}$$

The verticies must be ordered clockwise or counterclockwise; if they are ordered clockwise, the area will be negative but correct in absolute value.

The centroid (or geometric center) of a plane figure is the intersection of all straight lines that divide the 2D shape into two parts of equal moment about the line. For a non-self-intersecting (simple) polygon, with n vertices, the coordinates of the centroid are given by

$$\begin{aligned} C_x &= \tfrac{1}{6A}\textstyle\sum_{i=0}^{n-1}(x_i + x_{i+1})(x_i y_{i+1} - x_{i+1} y_i) \\ C_y &= \tfrac{1}{6A}\textstyle\sum_{i=0}^{n-1}(y_i + y_{i+1})(x_i y_{i+1} - x_{i+1} y_i) \end{aligned} \tag{4.3}$$

where A is the area (Burke, 1988). The verticies must be ordered clockwise or counterclockwise; if they are ordered clockwise, the coordinates of the centroid will be negative but correct in absolute value. The sum of all the distances from each vertex to the centroid for a 2D shape can be written

generally as

$$C = \sum_{i=0}^{n-1}((x_i - C_x)^2 + (y_i - C_y)^2)^{\frac{1}{2}}. \tag{4.4}$$

4.4.2 Iterative Solution Procedure

The gradients of the perimeter, $\mathbf{g}_p$, the area, $\mathbf{g}_a$, and the total distance from each vertex to the centroid, $\mathbf{g}_c$, can be calculated in *Matlab* using the *Symbolic Toolbox* function (See Appendix E) (Matlab, 2005). Therefore, for a model consisting of a collection of line segments, the gradient for the perimeter and area as well as the total distance from each vertex to the centroid will each be a column matrix. The number of rows in this matrix will be equivalent to the number of model parameters (i.e. the x and y position of each vertex as well as the velocities of the host rock and the deposit) being sought, the last two of which will be zero as velocity is not incorporated into either Equation 4.1, Equation 4.2, or Equation 4.4.

Similarly, the Hessian of the perimeter, $\mathbf{H}_p$, the area, $\mathbf{H}_a$, and the total distance from each vertex to the centroid, $\mathbf{H}_c$, can also be calculated in *Matlab* using the *Symbolic Toolbox* function (See Appendix E) (Matlab, 2005). Therefore, for a model consisting of a collection of line segments, the Hessian will consist of an m-by-n matrix where both m and n will be equivalent to the number of model parameters being sought. The last two columns and rows of each Hessian matrix will be zero as velocity is not incorporated

into either Equation 4.1, Equation 4.2, or Equation 4.4.

The Hessian and gradient matricies discussed above are substituted for $\mathbf{W}_x^T\mathbf{W}_x + \mathbf{W}_z^T\mathbf{W}_z$ and $\mathbf{W}_x^T\mathbf{W}_x\mathbf{m} - \mathbf{W}_z^T\mathbf{W}_z\mathbf{m}$, in Equation 2.24, respectively. Temporarily ignoring the matrix $\mathbf{W}_d$ in Equation 2.24 and rearranging, the solution to the inverse problem can be written iteratively as

$$\mathbf{m}^{s+1} = \mathbf{m}^s + \alpha(\mathbf{J}_r^T\mathbf{J}_r + \lambda(\mathbf{H}_p + \mathbf{H}_a + \mathbf{H}_c))^{-1}(\mathbf{J}_r^T(\mathbf{d}^{obs} - \mathbf{d}^{prd}) \\ -\lambda(\mathbf{g}_p + \mathbf{g}_a + \mathbf{g}_c)) \tag{4.5}$$

where $\mathbf{m}$ are the model parameters being sought in the inversion (i.e. the x and y coordinates of each vertex as well as the velocity of the host rock and ore deposit), $J_{ij} = \frac{\partial r_i}{\partial \mathbf{m}_j}$ are entries of the Jacobian $\mathbf{J}_r$, $\mathbf{d}^{obs}$ and $\mathbf{d}^{prd}$ are the observed and predicted travel-times, respectively. λ is varied until the trial model is such that the data misfit is small enough given the noise that was added into the data (See Chapter 2).

4.4.3 Results

Figure 4.9 shows the subsequent numerically defined surface inversion of a ten segment velocity model involving only the perimeter as the measure of model structure (See Appendix D). The starting model is shown in Figure 4.6. The resultant velocity model has a value of 2615 m/s, which is very similar to the synthetic one. Both the synthetic and calculated travel-times

are virtually identical. Additionally, the inversion process has converged to a minimum as there were no further changes in the model parameters with subsequent iterations. Therefore, minimizing the perimeter in conjunction with the data misfit is an acceptable approach to the inversion of a 2D ten segment polygon.

The majority of the computation time is spent adjusting the background velocity of the resultant (or inverted) model as for the example in Section 4.3.2. This is likely due to the large effect the background velocity has on the data misit. More specifically, a small perturbation in the background velocity has a dramatic effect on the travel time of a ray so the algorithm is forced to slowly change this feature. Figure 4.10 shows the exact same inversion except the background (or host rock) velocity is no longer a model parameter being sought and is instead known. As compared to Figure 4.9, the deposit has a velocity of 2521 m/s and is therefore more accurately depicted, however, the number of iterations is increased by 50. The perimeter trace is also less well behaved and while the kidney-bean shape is retained, the resultant velocity model is not as "smooth" as in Figure 4.9.

Ten segments worked nicely, however, it would be interesting to see how the procedure holds up to additional line segments. Also, more line segments have the advantage of finer discretization and thus a more detailed model. The exact same minimum structure inversion (including the unknown velocity) involving the perimeter was implemented for a twenty segment polygon (Figure 4.11). At iteration 35, two verticies switched postions and the resul-

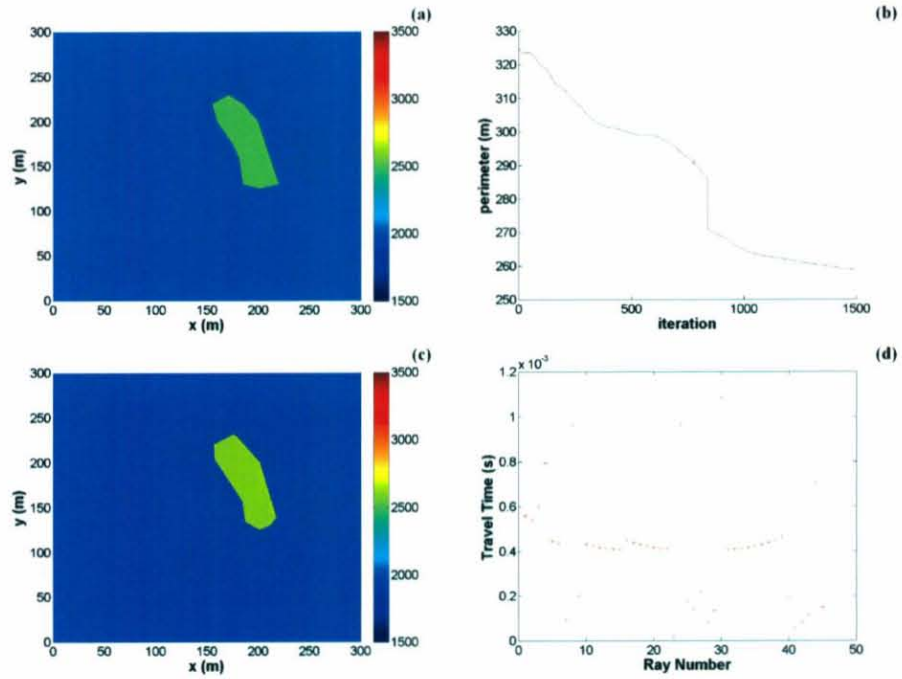

Figure 4.9: Two-dimensional minimum structure (perimeter) inversion results for a ten segment model: (a) Synthetic velocity model. (b) Resultant velocity model perimeter trace. (c) Resultant velocity model. (d) Difference between calculated (i.e. inverted) travel-time and synthetic travel-time.

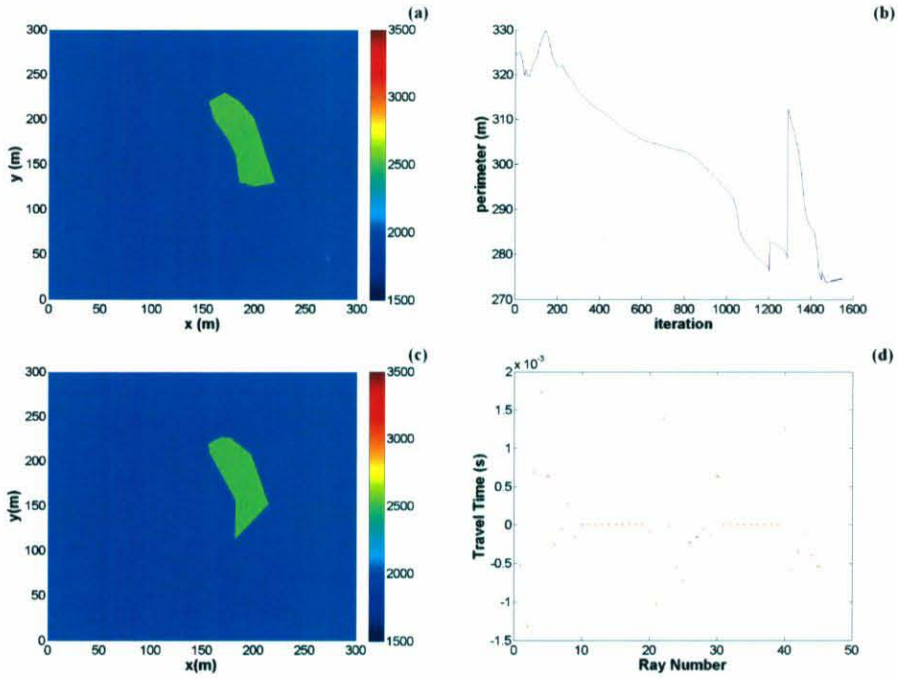

Figure 4.10: Two-dimensional minimum structure (perimeter) inversion results for a ten segment model (background velocity known): (a) Synthetic velocity model. (b) Resultant velocity model perimeter trace. (c) Resultant velocity model. (d) Difference between calculated (i.e. inverted) travel-time and synthetic travel-time.

tant velocity model turned "inside out". Specifying the background velocity and removing it from the set of model parameters being sought allows the algorithm to continue for a greater number of iterations (i.e. 229) but without a substantial improvement in the solution obtained (Figure 4.12).

From Figure 4.11, it is obvious that the perimeter alone will not suffice in controlling the inversion process for more complex (i.e. greater number of line segments) 2D models. An additional measure of model structure must therefore be introduced.

The area A of a polygon (Equation 4.2) can also be computed if the lengths of the sides, $a_1, a_2, ..., a_n$ and the exterior angles, $\theta_1, \theta_2, ..., \theta_n$ are known (Figure 4.13). The formula is given by: (Lopshits, 1963)

$$\begin{aligned} A = \frac{1}{2}(a_1[a_2 sin(\theta_1) + a_3 sin(\theta_1 + \theta_2) + \cdots + a_{n-1} sin(\theta_1 + \cdots + \theta_{n-2})] \\ + a_2[a_3 sin(\theta_2) + a_4 sin(\theta_2 + \theta_3) + \cdots + a_{n-1} sin(\theta_2 + \cdots + \theta_{n-2})] \\ + \cdots + a_{n-2}[a_{n-1} sin(\theta_{n-2})]) \end{aligned} \tag{4.6}$$

Figure 4.14 illustrates the change in the external angle of the involved line segments when part of a polygon flips inside-out during an inversion. According to Equation 4.6, the area is related to the external angles of all the line segments. Therefore, in order to prevent this flipping of vertices from occuring, the area is an acceptable form of model structure to be minimized alongside the perimeter.

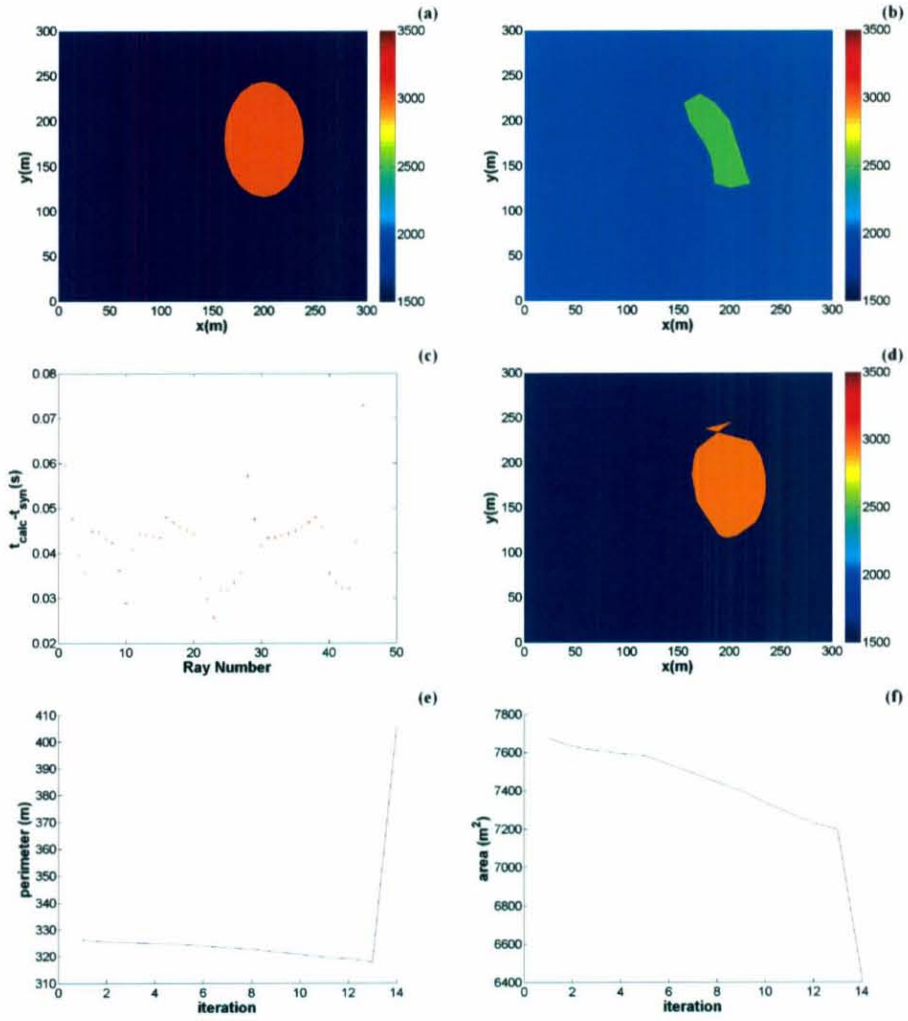

Figure 4.11: Two-dimensional minimum structure (perimeter) inversion results for a twenty segment model: (a) Initial velocity model. (b) Synthetic velocity model. (c) Difference between calculated (i.e. inverted) travel-time and synthetic travel-time. (d) Resultant velocity model. (e) Perimeter trace. (f) Area trace.

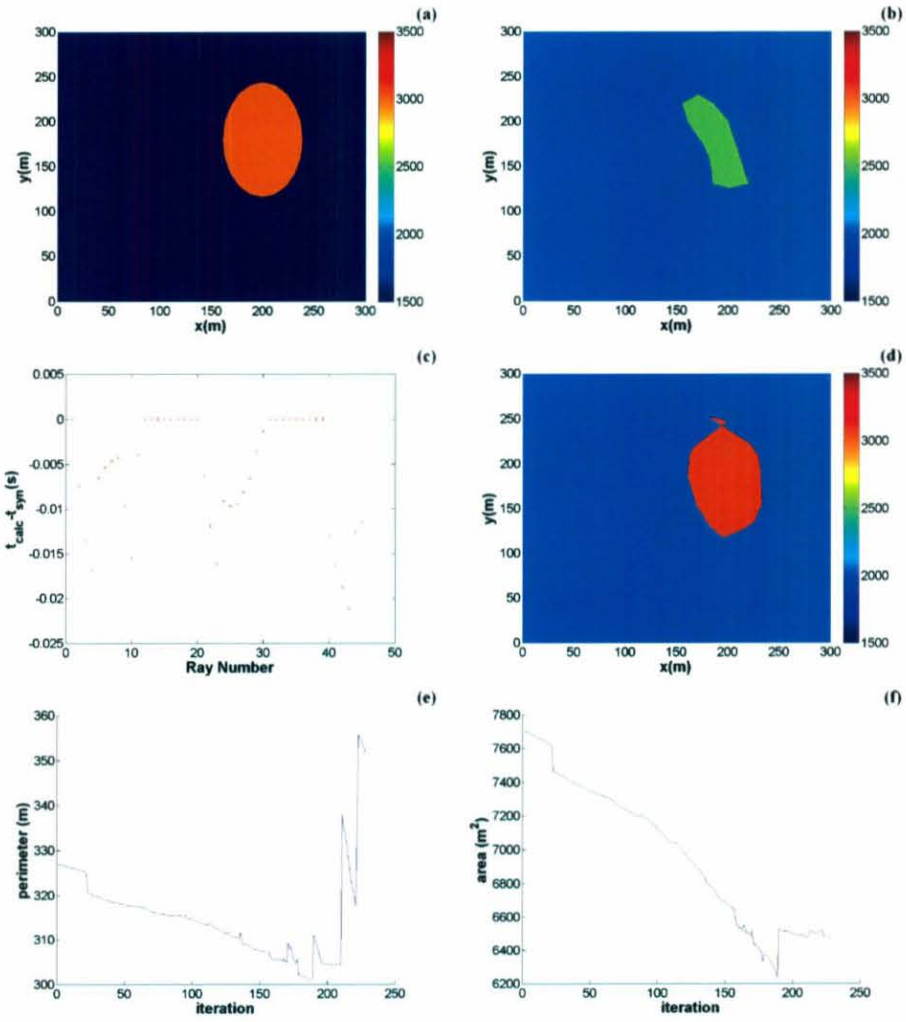

Figure 4.12: Two-dimensional minimum structure (perimeter) inversion results for a twenty segment model (background velocity known): (a) Initial velocity model. (b) Synthetic velocity model. (c) Difference between calculated (i.e. inverted) travel-time and synthetic travel-time. (d) Resultant velocity model. (e) Perimeter trace. (f) Area trace.

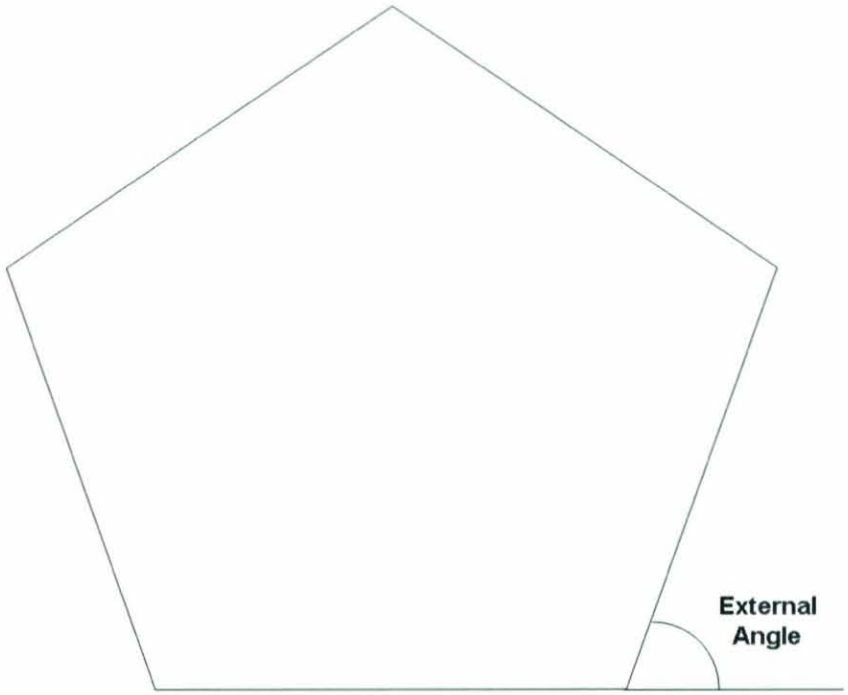

Figure 4.13: Schematic illustrating the external angle of a five sided polygon.

Minimizing the area alongside the perimeter prevents the polygon from flipping inside out but consequently shrinks the resultant velocity model (Figure 4.15). Manipulating the trade-off parameter with regards to the area proved extremely difficult. The "strength" afforded to the area via the trade-off parameter remained either too high or too low and a so-called middle ground could not be found.

Specifying the background velocity and removing it from the set of model parameters being sought does not prevent the resultant velocity model from

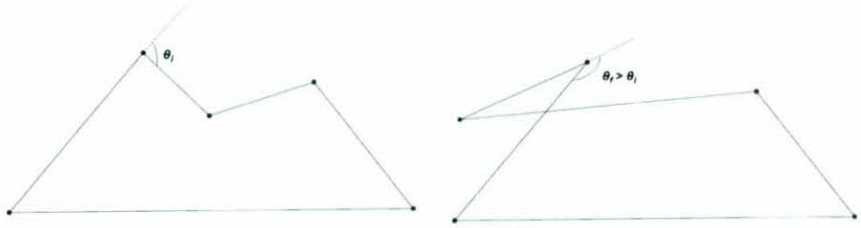

Figure 4.14: Schematic illustrating the change in the external angle of the involved line segments when a polygon flips inside during an inversion

shrinking (Figure 4.16). However, it does result in a smaller misift between the synthetic and calculated (or inverted) travel-times thereby creating the illusion of a better solution (Figure 4.17). A number of rays pass through the background (or host rock) without traveling through the anomaly. These rays are entirely influenced by the background velocity. Therefore, specifying this value leads to the apearance of a 'better' solution. This is an important point, which needs to be taken into consideration when interpreting any and all results.

Figures 4.15 and 4.16 show recovered models in which the anomaly appears with a velocity *lower* than the background, though the input velocity was substantially *faster* than the background. The reason for this is likely due to the fact the inversion algorithm got 'stuck' in a local minimum.

It is obvious from the previous examples that both the area and perimeter alone are not sufficiently useful measures of model structure. In order for the inversion to approach a more satisfactory and geologically plausible result, an additional property of a polygon must be considered.

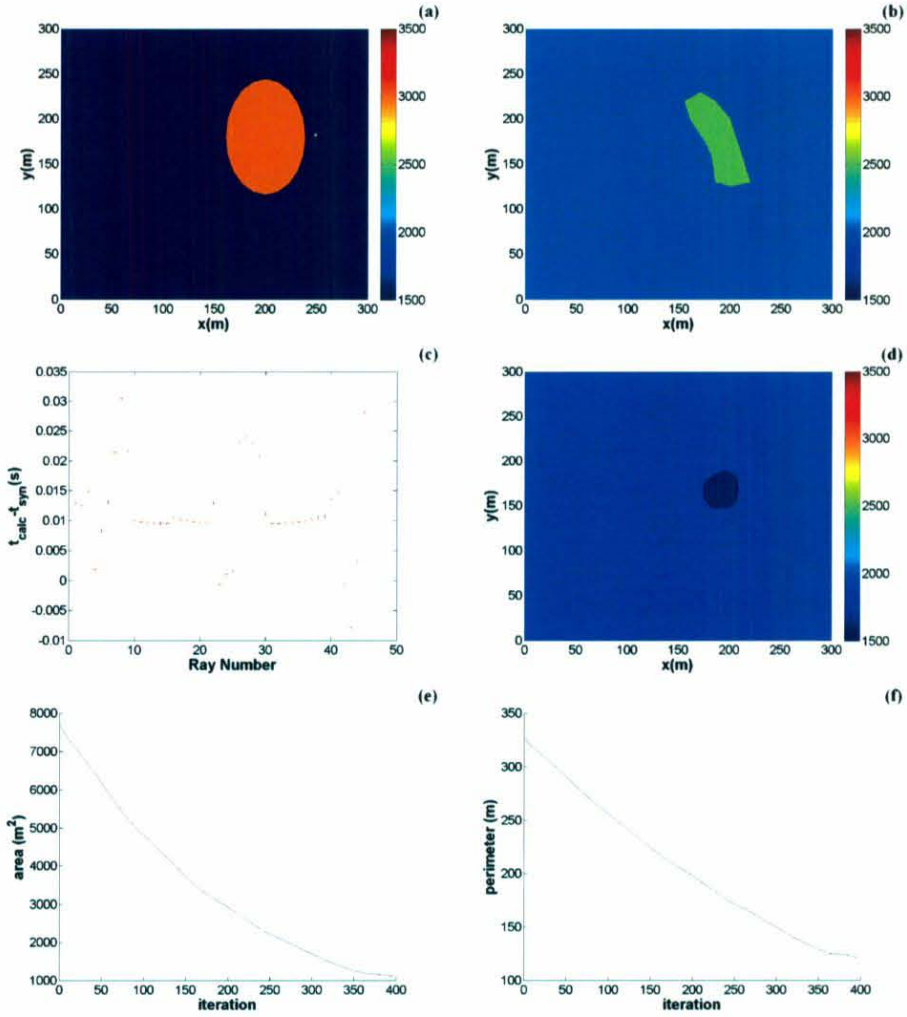

Figure 4.15: Two-dimensional minimum structure (perimeter and area) inversion results for a twenty segment model: (a) Initial velocity model. (b) Synthetic velocity model. (c) Difference between calculated (i.e. inverted) travel-time and synthetic travel-time. (d) Resultant velocity model. (e) Area trace. (f) Perimeter trace.

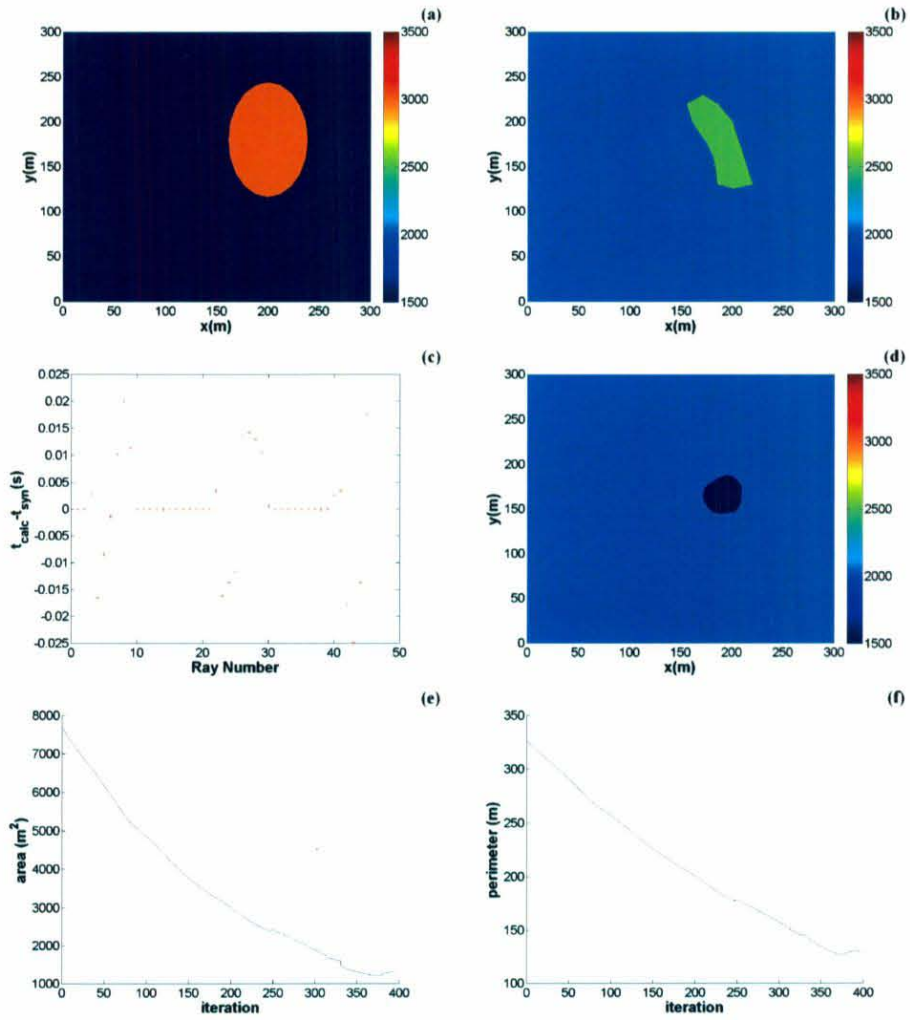

Figure 4.16: Two-dimensional minimum structure (perimeter and area) inversion results for a twenty segment model (background velocity known): (a) Initial velocity model. (b) Synthetic velocity model. (c) Difference between calculated (i.e. inverted) travel-time and synthetic travel-time. (d) Resultant velocity model. (e) Area trace. (f) Perimeter trace.

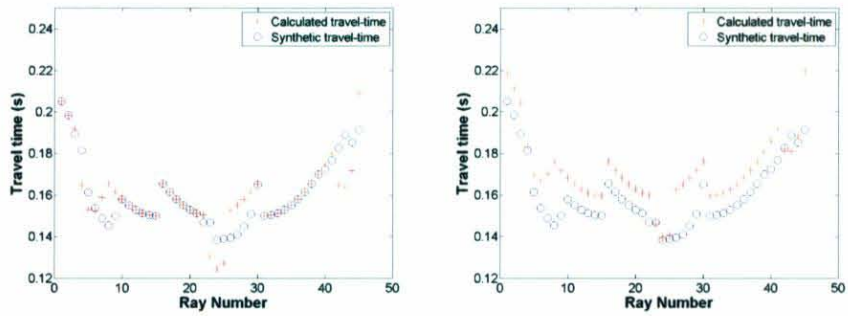

Figure 4.17: Calculated travel-time (blue circles) and predicted travel-time (red crosses) for a two-dimensional minimum structure (perimeter and area) inversion results for a twenty segment model (background velocity known) (*Left*) and background velocity unknown (*Right*).

Minimizing the sum of the lengths from each vertex to the centroid alongside both the perimeter and the area produces a much more robust and reliable inversion algorithm. As can be seen from Figure 4.18, the inversion process converges to a minimum, signified by the leveling off of the area, perimeter and total length to center traces. Additionally, the general shape of the resultant velocity model matches that of the synthetic model and both the calculated and synthetic travel-times correspond fairly well. Table 4.1 provides a comparison of multiple model properties for the synthetic and inverted velocity models.

The majority of the computation time is spent adjusting the background velocity of the resultant (or inverted) model. Figure 4.19 shows the exact same inversion except that the background (or host rock) velocity is no longer a model parameter being sought and is instead known. As compared to Figure 4.18, the velocity of the deposit is more accurately depicted and the

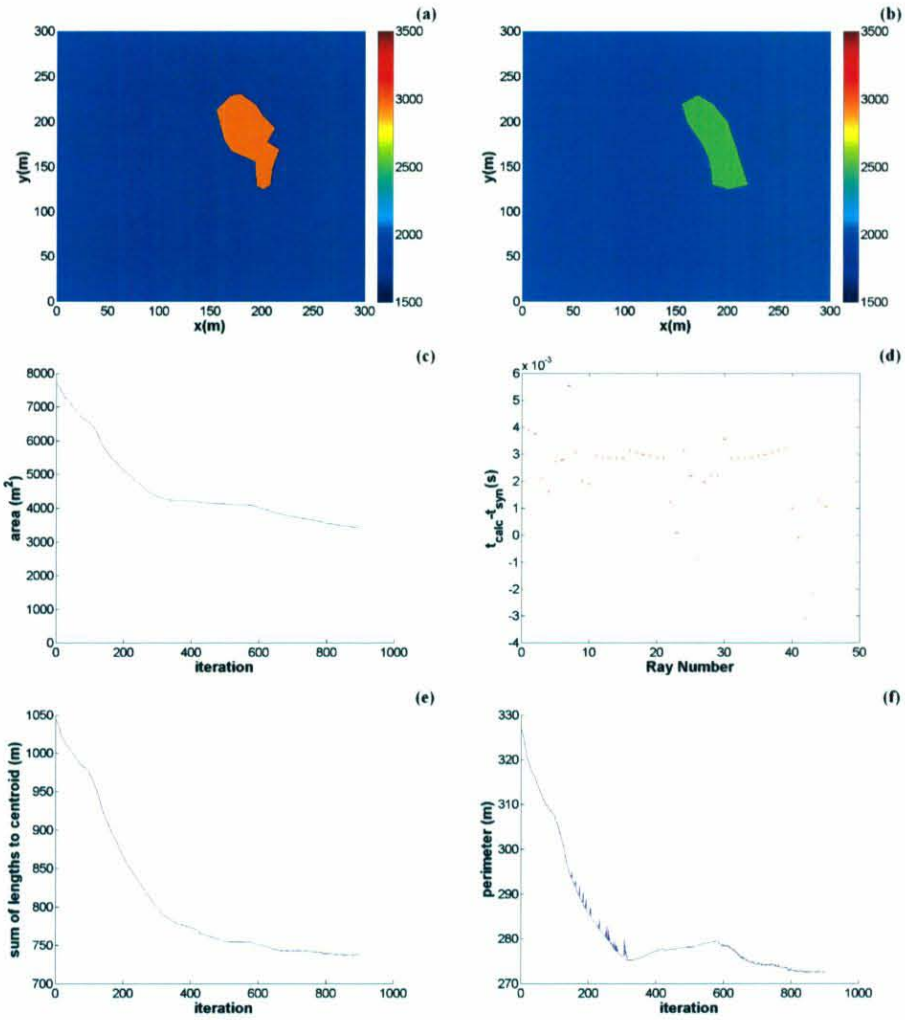

Figure 4.18: Two-dimensional minimum structure (perimeter, area and sum of lengths to centroid) inversion results for a twenty segment model: (a) Resultant velocity model. (b) Synthetic velocity model. (c) Area trace. (d) Difference between calculated (i.e. inverted) travel-time and synthetic travel-time. (e) Sum of the lengths of each vertex to the centroid trace. (f) Perimeter trace.

	Synthetic Model	Inverted Model
Perimeter	266.4	273.3
Area	3282	3459
Centroid	(188.3, 176.8)	(187.2,184.8)
Sum of Lengths to Centroid	732.1	739.4
Background Velocity	2000m/s	1962m/s
Deposit Velocity	2500m/s	2971m/s

Table 4.1: Comparison of the synthetic and inverted velocity models for a minimum structure inversion (perimeter, area and sum of lengths to centroid) of a twenty segment polygon

number of iterations decreased by 80. The misfit between the synthetic and calculated (or inverted) travel-times is also smaller (Figure 4.20). Table 4.2 provides a comparison of multiple model properties for the synthetic and inverted velocity models when the background velocity is a known parameter.

	Synthetic Model	Inverted Model
Perimeter	271.6	269.5
Area	3327	3379
Centroid	(184.7, 185.0)	(184.5,184.9)
Sum of Lengths to Centroid	736.2	741.0
Background Velocity	2000m/s	2000m/s
Deposit Velocity	2500m/s	2755m/s

Table 4.2: Comparison of the synthetic and inverted velocity models for a minimum structure inversion (perimeter, area and sum of lengths to centroid) of a twenty segment polygon (background velocity known)

The total-centroid-distance measure is essential for stabilizing the inversion. The measure cannot be used on its own without the perimeter/area measures as the resulting inversion is unstable. Figure 4.21 shows the resultant velocity model for a minimum structure inversion of a twenty segment

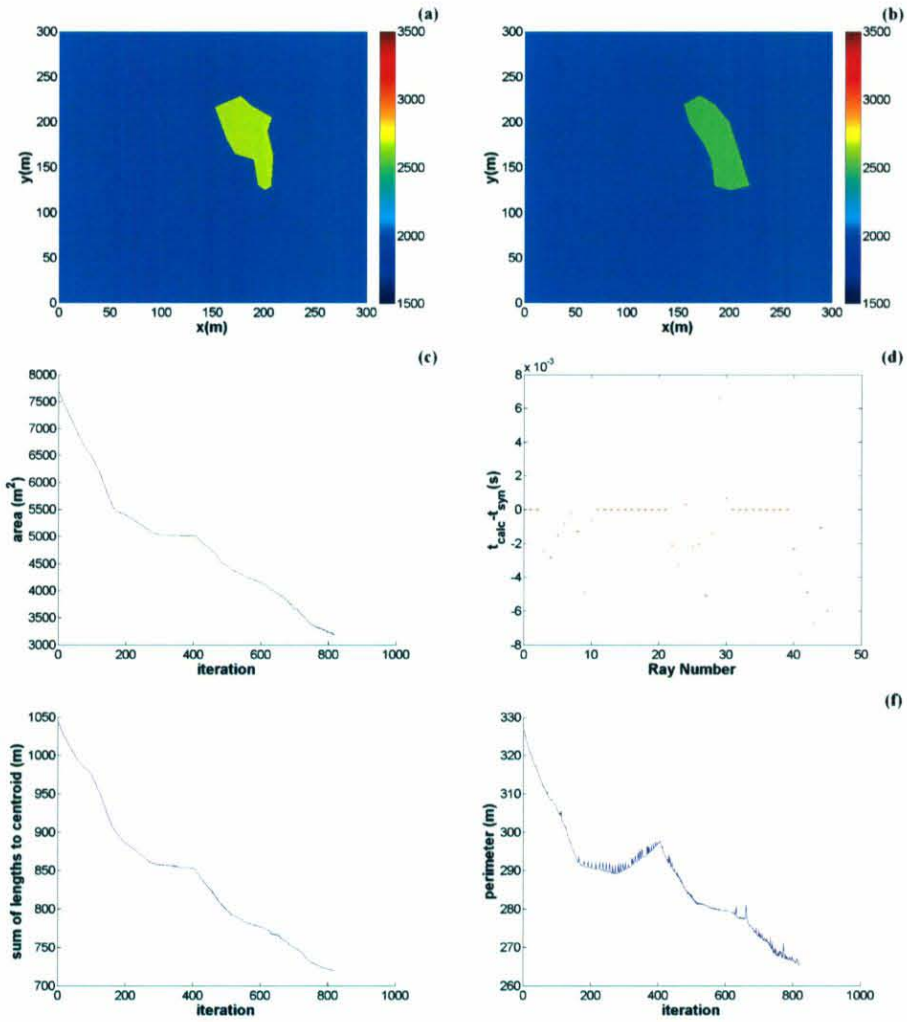

Figure 4.19: Two-dimensional minimum structure (perimeter, area and sum of lengths to centroid) inversion results for a twenty segment model (background velocity known): (a) Resultant velocity model. (b) Synthetic velocity model. (c) Area trace. (d) Difference between calculated (i.e. inverted) travel-time and synthetic travel-time. (e) Sum of the lengths of each vertex to the centroid trace. (f) Perimeter trace.

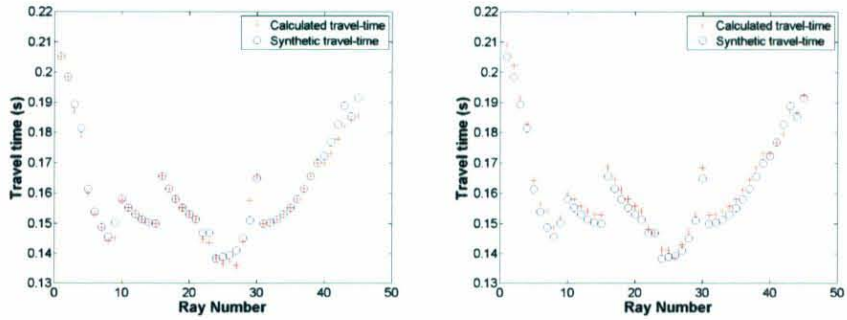

Figure 4.20: Calculated travel-time (blue circles) and predicted travel-time (red crosses) for a two-dimensional minimum structure (perimeter, area and sum of lenghts to the centroid) inversion results for a twenty segment model (background velocity known) (*Left*) and background velocity unknown (*Right*).

polygon with only the sum of lengths to the centroid used as a measure of model structure. The model bears no resembalance to the synthetic model shown in Figure 4.18 (b) and on close inspection has actually flipped in on itself. All three measures of model structure are needed as they work in unision to help stabalize the inversion.

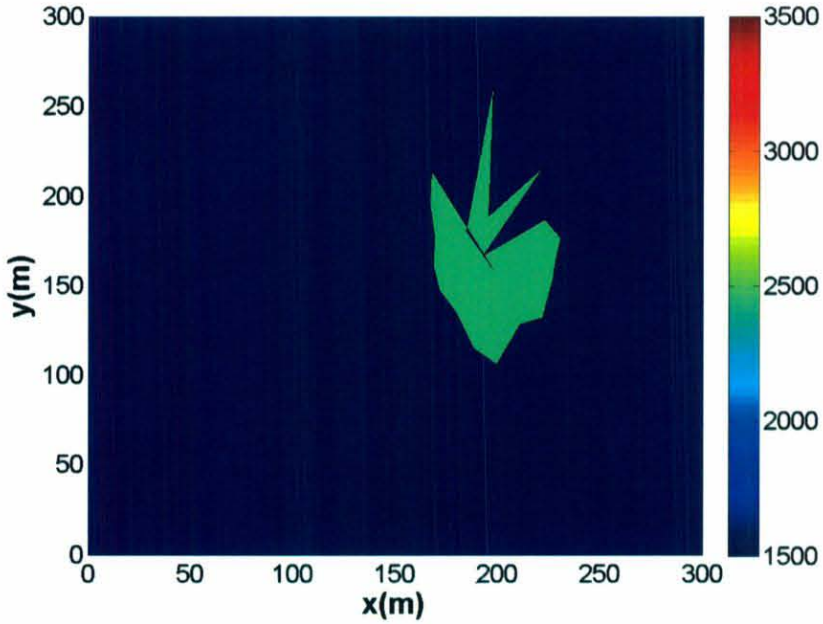

Figure 4.21: Two-dimensional minimum structure inversion result for a twenty segment model using only total-centroid-distance as a measure of model structure.

Chapter 5

Numerically Defined Surface (3D)

5.1 Model Parametrization

Arbitrary 3D shapes are often too complicated to analyze via a single mathematical formula and so are divided (tessellated) into a mesh of small, easy-to-analyze triangular facets. For example, consider first a simple sphere (Figure 5.1). The tessellation algorithm uses recursive subdivision (Matlab, 2005). The first approximation is a platonic solid, either an icosahedron, octahedron or a tetrahedron (Matlab, 2005). Each level of refinement subdivides each triangular facet by a factor of 4 (Matlab, 2005). At each refinement, the vertices are projected to the surface of the sphere (See Appendix F). In order to generate a more general initial model, the vertices of the triangular planes will be varied randomly by hand while keeping the tessellation intact. The position of all vertices and the velocities of both the deposit and host rock will be the model parameters sought in the inversion.

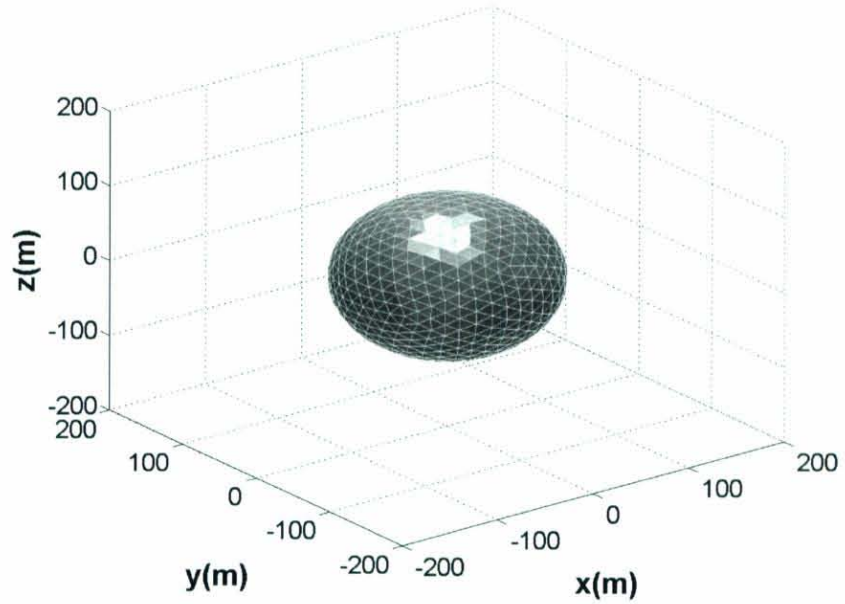

Figure 5.1: Tessellated sphere (radius=100m) containing 1280 triangles.

5.2 The Forward Problem

As discussed previously, the primary interest of this paper is model parametrization as it applies to the inversion procedure. Therefore, we simplify both the forward and inverse problems by assuming a linear raypath from source to reciever. Under the straight ray approximation, all directional changes attributed to velocity variations are ignored.

Assuming a generally convex outward shape defined via a collection of triangular facets in 3D, seismic rays will only be traveling through a maximum of two interfaces.

Figure 5.2 shows the resultant ray paths through a 2500m/s subsurface tesselated sphere of radius 100m consisting of 80 triangular facets. Sources are shown in red and receivers in green. There are 3 source and receiver boreholes each containing 3 sources and 26 receivers, respectively. This provides a total of 702 rays, which are numbered first from the top to bottom of the borehole and then along the positive x-axis starting at $x = 100m$. The source and receiver configurations shown will be used for all of the subsequent examples involving 3D numerically defined surfaces. The intersection points for each ray were first calculated. Next, the distances corresponding to the host rock and the deposit were determined and subsequently multiplied by the appropriate velocity in order to determine the travel time for each ray (Figure 5.3) (See Appendix G).

There are no doubt many instances for which the straight ray approximation may not be appropriate nor desired. Before abandoning the forward problem all together a couple of approaches to ray tracing, namely the shooting method and the minimization of travel time, will be discussed although they won't be used in the inverse problem.

5.2.1 Shooting Method

Figure 5.4 shows an incoming ray (marked **I**) striking a surface with normal **N**. The incident ray makes an angle θ_i (the *angle of incidence*) with the surface normal. The transmitted ray **T** makes an angle θ_t (the *angle of refraction*) with the reflected normal. The incident ray, normal and refracted

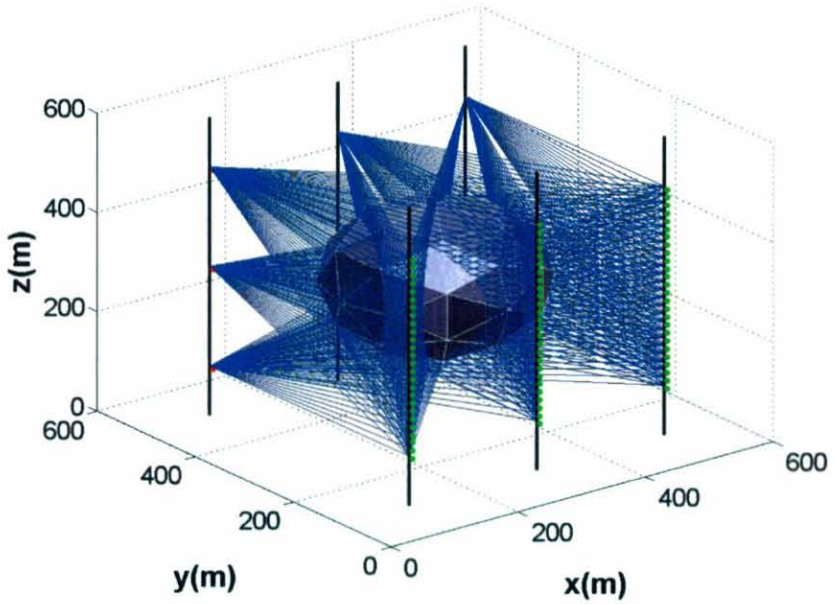

Figure 5.2: Resultant ray paths through a 2500m/s subsurface tessellated sphere of radius 100m consisting of 80 trianglular facets embedded in a 2000m/s host rock. Sources are shown in red and receivers in green.

ray all lie in the same plane (Glassner, 1989). The equation relating the angles of the incident and transmitted ray is called *Snells Law*:

$$\frac{\sin(\theta_1)}{v_1} = \frac{\sin(\theta_2)}{v_2} \tag{5.1}$$

where v_1 is the velocity of medium 1 and v_2 is the velocity of medium 2.

The shooting-method is an iterative procedure that uses standard initial-value ray tracing to solve a boundary-value ray tracing problem (Červaný, 2001). The shooting method is ideal for situations in which we need to

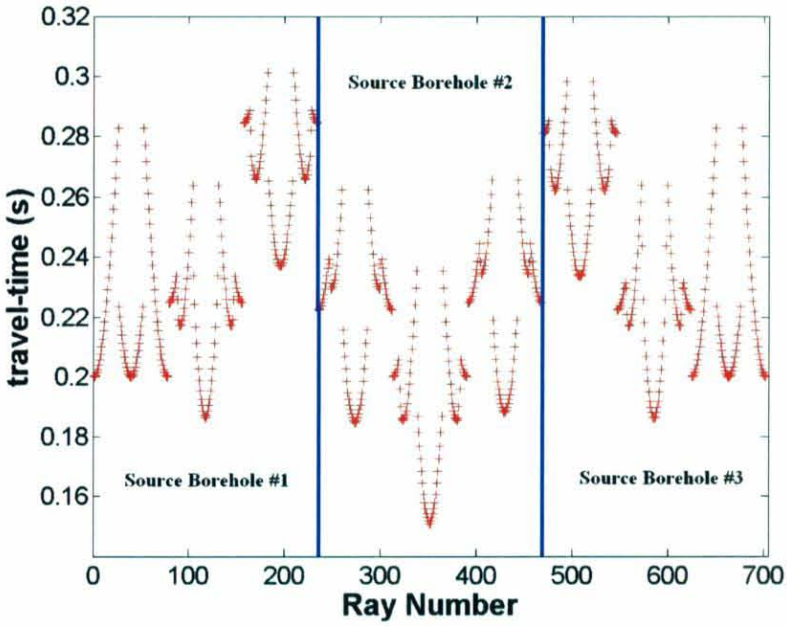

Figure 5.3: Associated travel-time for Figure 5.2 organized according to source borehole.

find rays from a point source to a series of recievers distributed regularly or irregularly in some region along the surface of the earth or vertically in a borhole. We start shooting rays that hit the Earth's surface (or subsurface when in a borehole) outside the region of recievers. Upon encountering an interface, any directional changes due to velocity variations can be calculated quickly and simply using Equation 5.1. The take-off angle is then varied regularly in order to come closer to the reciever region. Figure 5.5 illustrates the shooting method for two planar interfaces and a single point source (See Appendix G).

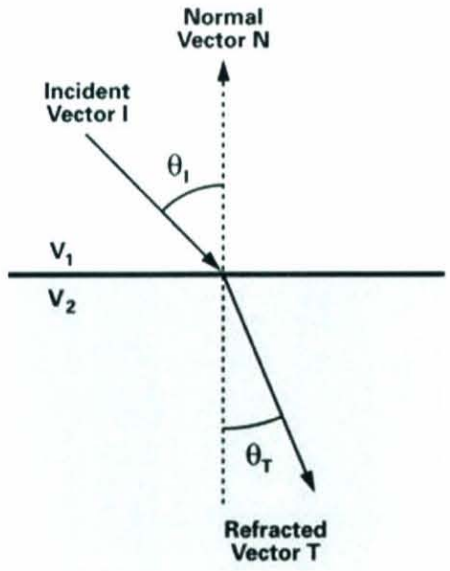

Figure 5.4: The geometry of transmission (After Glassner, 1989)

5.2.2 Minimization of Travel-time

Fermat's principle states that a wave will take a raypath for which the travel-time is stationary with respect to minor variations of the raypath (Sheriff & Geldart, 1995). For most situations, this raypath is the one that requires the least time (Sheriff & Geldart, 1995). Snell's law, Huygens' principle, and many other laws of geometrical optics can be derived from this principle (Sheriff & Geldart, 1995). An obvious consequence of this principle is that paths of light/seismic energy traveling in a homogeneous medium are straight lines, as a straight line is the shortest distance between two points.

Following Chander (1975), let P_1 to P_{n+1} in Figure 5.6 be the consecutive vertices of a refracted seismic ray with P_1 representing the source and P_{n+1}

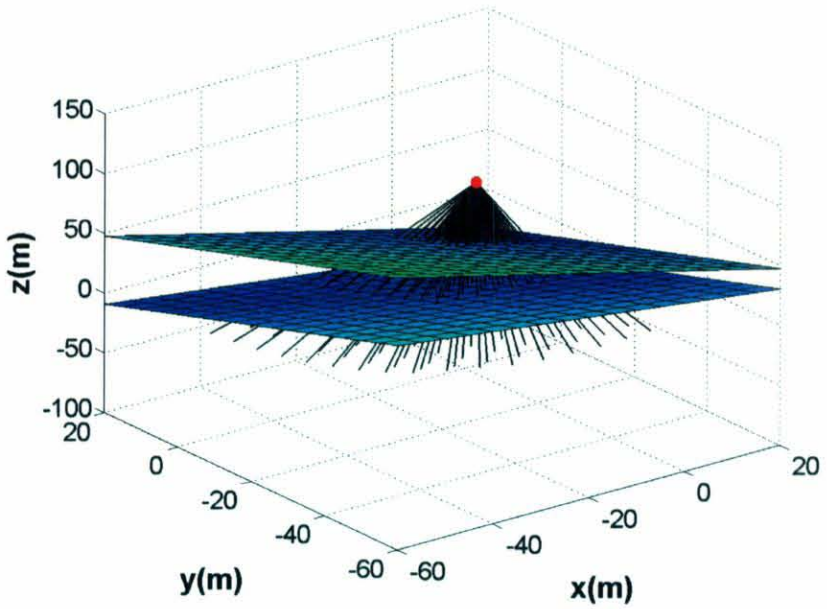

Figure 5.5: Schematic illustrating the shooting method for two planar interfaces and a single point source (red)

the receiver. Let (x_i, y_i, z_i), where i = 1, ..., n+1, be the coordinates of these vertices, respectively. The travel time t along the ray is given by:

$$t = \sum_{i=2}^{n+1} [(x_i - x_{i-1})^2 + (y_i - y_{i-1})^2 + (z_i - z_{i-1})^2]^{1/2} v_i^{-1} \tag{5.2}$$

where v_i (i = 1, ..., n+1) is the constant velocity between interfaces IF_{i-1} to IF_i (i = 2, ..., n+1). In order to determine the path a ray will take, we minimize Equation 5.2 (as per Fermat's principle). The coordinates (x_1, y_1, z_1) and (x_{n+1}, y_{n+1}, z_{n+1}) of the source and receiver must be known in order to successfully trace a ray. This optimization problem is nonlinear and must

be constrained by the fact that each refraction point lies somewhere on the surface of the interface through which it is traveling. The minimization procedure was created and carried out in Mathematica using Newton's Method (Mathematica, 2005) (See Appendix G).

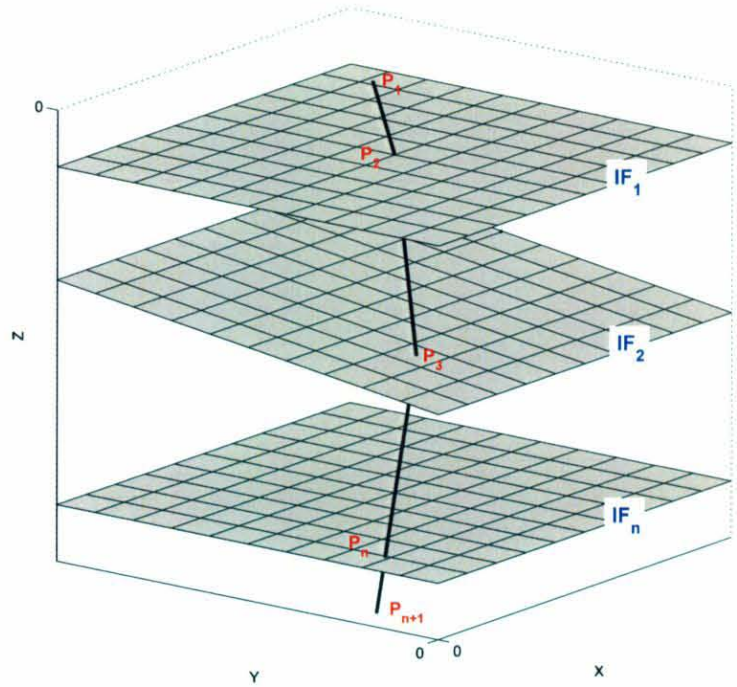

Figure 5.6: Schematic diagram showing a refracted ray traveling between source P_1 and receiver P_{n+1}. P_2 to P_n are intervening vertices numbered in order as encountered when proceeding along the ray from source to receiver. IF_1, IF_2, ..., IF_n are plane interfaces separating layers of constant velocity.

We are interested in tracing rays through subsurface ore deposits in order to determine travel times which can be inverted to give information on the

deposit's structural orientation and physical properties. These deposits can be modelled as complex enclosed 3D shapes represented via a collection of triangular facets. As discussed above, we first solve the forward problem for a tessellated sphere. Tessellating a complex 3D shape significantly decreases the complexity of the optimization procedure as we are tracing rays through planes and not curved interfaces.

The full ray tracing problem for a tessellated sphere involves first choosing a single triangular facet at random. This facet is then paired with one of the remaining facets and a ray is traced through both for a specified source and receiver position by minimizing the travel time in an analogous manner to that of Chander (1975) described above. The minimization procedure is based on the interior-reflective Newton Method and was written and executed in Matlab (Matlab, 2005) (See Appendix G). It was then determined if the subsequent refraction points for the resulting ray actually lay within the choosen triangular facets. If this was the case, the travel time was recorded and a new initial triangular facet was chosen so that the process could be repeated for another ray. However, if the refraction points happened not to lie within either of the triangular facets, the second one would be discarded and a new one chosen until a suitable match was found.

A number of boundary conditions had to be implemented in order to ensure each ray behaved as intended. First, instead of refracting through the second interface, a number of rays were reflected or experienced critical refraction and then were reflected towards the interior of the tessellated sphere

(Figure 5.7). Since the minimization algorithm was only programmed to contend with a maximum of two interfaces, these rays were allowed to pass through a third interface unaffected. To prevent this from happening, every ray was forced to enter a facet in the opposite direction of its outward normal and leave in the same direction. Next, a method had to be devised to ensure that each refraction point did indeed lie within the specified triangular plane. This was accomplished by comparing the area of the specified triangle (A_T) with the combined area of the three triangles formed by drawing a line from each vertex to the refraction point (A_1+A_2+A_3) (Figure 5.8). Only when these two values were equal would the refraction point be accepted as real.

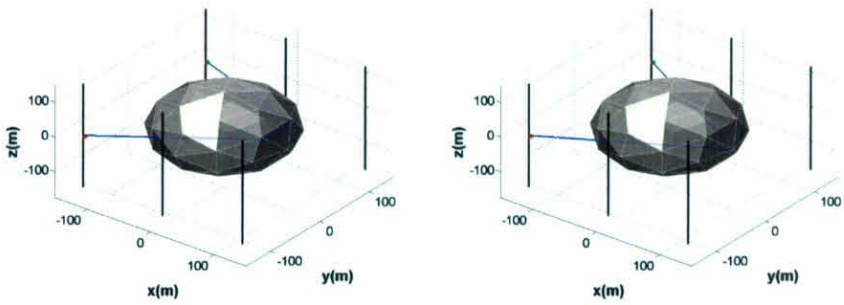

Figure 5.7: *Left*: example of a critically refracted ray being passing through a third interface unaffected. *Right*: example of a reflected ray passing through a third interface unaffected.

The first attempt at tracing rays through Figure 5.1, although successful, proved too computationally expensive (on the order of 43,200 seconds or twelve hours on a standard 1.83GHz Intel Core 2 Dell laptop). The majority of this time was spent minimizing the travel time between unsuccesful

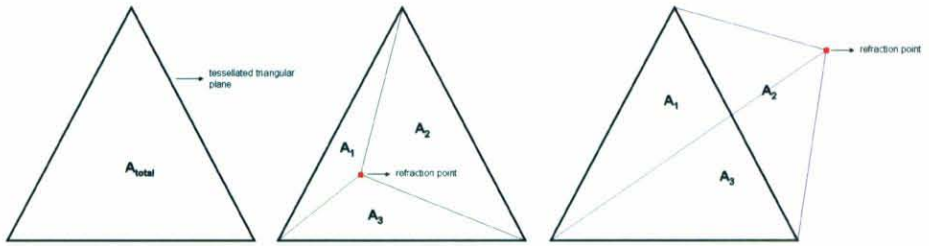

Figure 5.8: Schematic of tessellated triangular facet illustrating the method used to determine if a refraction point lay on the surface of a specified plane.

facet pairs. In order to rectify this problem, the ray tracing algorithm was provided with initial estimates of correct facet pairs. These estimates were obtained by first tracing a ray through a sphere of equal diameter (Figure 5.9) (See Appendix G). The minimization algorithm searched the triangular facets surrounding the initial estimate until a match was found. By providing these initial estimates, the computation time was significantly reduced (approximately 7000 seconds or just less than 2 hours). The resultant ray paths through the tessellated sphere for numerous source and reciever pairs are shown in Figure 5.10.

The ray paths through the tessellated sphere shown in Figure 5.10 do not precisely correspond to those through a sphere of equal diameter. The tessellation causes a deviation from a true spherical shape resulting in slightly different ray paths. This being said, the travel times of the rays through the tessellated sphere and the sphere of equal diameter are very similar (Figure 5.11) and the coverage is the same. Increasing the number of triangles will decrease the difference in ray paths accordingly but will not have a major

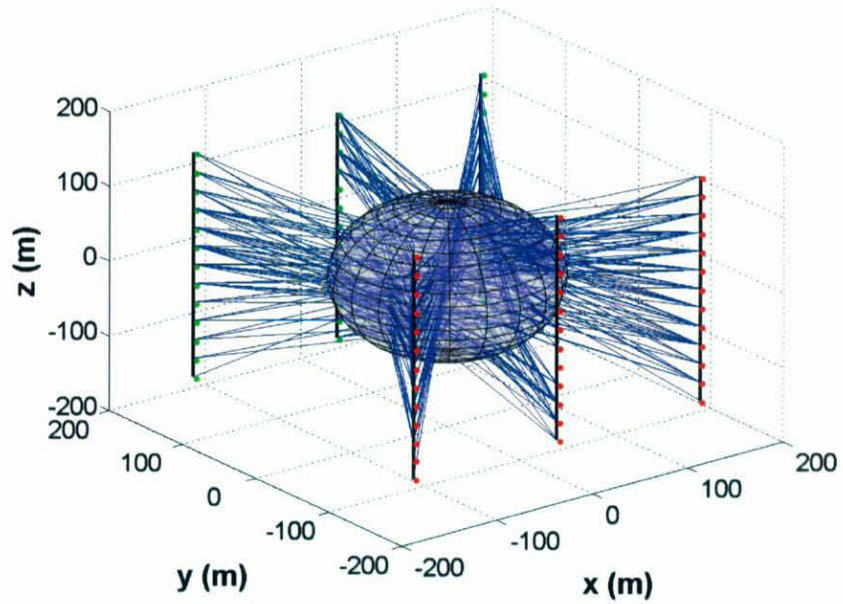

Figure 5.9: Resultant ray paths through a sphere equal in diameter to the tesselated sphere shown in Figure 5.1. The refraction points of these rays were used as initial estimates for tracing rays through a tessellated sphere of equal diameter. The sources are shown in red and the receivers in green.

affect on the results obtained.

To reiterate, this approach to the ray tracing was not used for the inversion in this thesis as it proved too time consuming. Instead, the forward problem was simplified by assuming all rays traveled in a straight line from source to reciever.

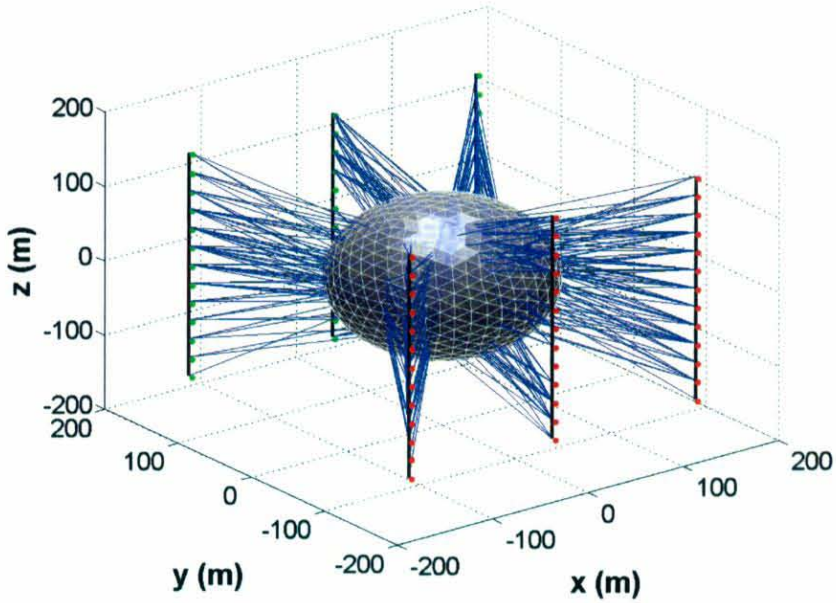

Figure 5.10: Resultant ray paths through a tessellated sphere of radius 100m and consisting of 1280 triangular facets using the initial estimates obtained by tracing rays through a sphere of equal diameter. The sources are shown in red and the receivers in green.

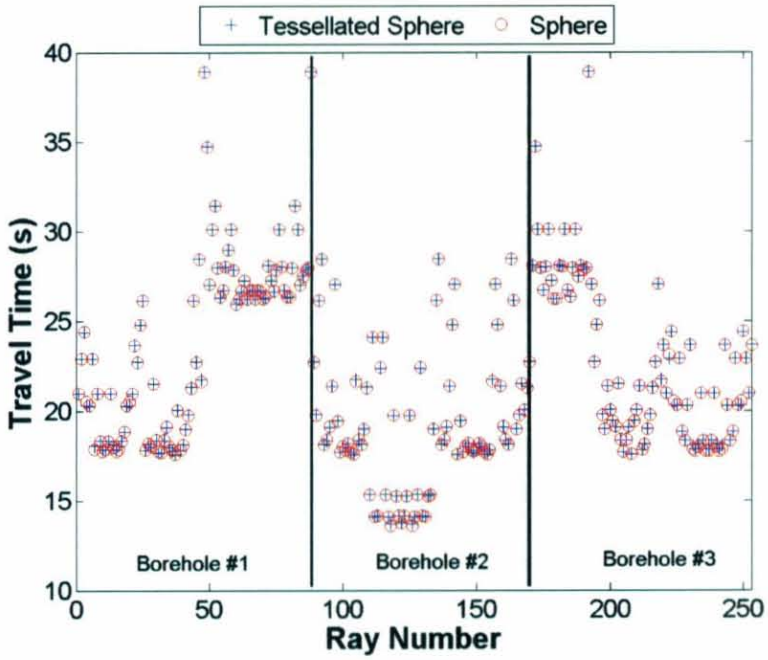

Figure 5.11: Comparison of the travel times of ray paths through a tessellated sphere (crosses) and a sphere (circles) of equal radius. Borehole #1, Borehole #2 and Borehole #3 correspond to all ray paths involving a source located at x=*-150*,x=*0* and x=*150*, respectively.

5.3 Minimum Structure Inversion of a Numerically Defined Surface Model

5.3.1 Measures of Model Structure

The solution to the inverse problem in three-dimensions will follow the minimum structure method outlined in Chapter 4 for 2D models. The major difference will be in using 3D equivalents to the 2D area, perimeter and total distance from each vertex to the object's centroid.

The perimeter will now be defined as the sum of the perimeter of each triangular facet and can be written numerically as follows

$$P_t = \sum_{i=1}^{n+1}(((x_2 - x_1)^2 + (y_2 - y_1)^2 + (z_2 - z_1)^2)^{1/2} + ((x_3 - x_2)^2 + (y_3 \quad (5.3)$$
$$-y_2)^2 + (z_3 - z_2)^2)^{1/2} + ((x_1 - x_3)^2 + (y_1 - y_3)^2 + (z_1 - z_3)^2)^{1/2})_i,$$

where i represents subsequent triangular facets.

The centroid $\mathbf{C}$ of a 3D object made up of a collection of $\mathbf{N}$ triangular faces with vertices (a_i, b_i, c_i) can be written as (Burke, 1988)

$$\frac{\sum_{i=0}^{n-1} A_i R_i}{\sum_{i=0}^{n-1} A_i}. \quad (5.4)$$

R_i is the average of the vertices of the i'th face and is given by (Burke, 1988)

$$\frac{(a_i + b_i + c_i)}{3}. \tag{5.5}$$

A_i is twice the area of the i'th face and can be written as (Burke, 1988)

$$\|(b_i - a_i) \times (c_i - a_i)\|. \tag{5.6}$$

The sum of all the distances from each vertex to the centroid for a 3D shape made up of collection of **N** triangular faces can be written generally as

$$\sum_{i=0}^{n-1}((x_i - C_x)^2 + (y_i - C_y)^2 + (z_i - C_z)^2)^{\frac{1}{2}}. \tag{5.7}$$

The parallelogram determined by the vectors **u** and **v** has base length $\|\mathbf{v}\|$ and altitude $\|\mathbf{u}\| \sin\theta$ (Figure 5.12)(Nicholson, 2003). Hence the area of a parallelogram formed by **u** and **v** is

$$(\|\mathbf{u}\| \sin\theta)\|\mathbf{v}\| = \|\mathbf{u} \times \mathbf{v}\|. \tag{5.8}$$

The area of a triangle is half the area of a parallelogram determined by these vectors and is given by

$$\frac{1}{2}\|\mathbf{u} \times \mathbf{v}\|. \tag{5.9}$$

In terms of a measure of model structure, the areas for each triangular facet will be summed as follows

$$\sum_{i=0}^{n-1}(\frac{1}{2}\|\mathbf{u}\times\mathbf{v}\|)_i, \tag{5.10}$$

where i represents subsequent triangular facets.

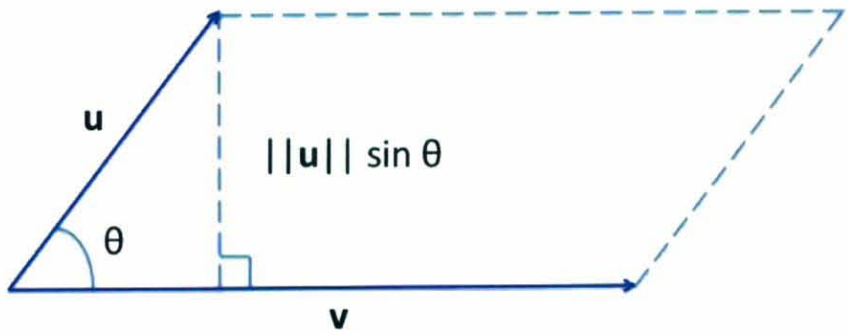

Figure 5.12: The vectors **u** and **v** form adjacent sides of a parallelogram (After Nicholson, 2003).

5.3.2 Iterative Solution Procedure

The gradient and Hessian of the total perimeter, P_t, the total area, A_t, and the total distance from each vertex to the centroid, C_t, were again calculated using *Matlab* (Matlab, 2005) (See Appendix H) (See Section 4.4.2).

The solution to the inverse problem can be obtained by substituting the appropriate gradients and Hessians for the 3D case into Equation 4.5. The model parameters, **m**, being soug!ht in the inversion are the x, y and z coordinates of each vertex as well as the velocity of the host rock and ore deposit. Again, rays are assumed to go straig!ht from source to reciever regardless of velocity variations.

One major drawback to this iterative solution procedure is computation time. The inversion of a moderately complex set of data for a velocity model consisting of 80 triangular facets took approximately 30 days on a standard 1.83GHz Intel Core 2 Dell laptop. While this proved frustrating, it had no bearing on the results.

5.3.3 Results

Minimizing the total perimeter, the total area and the total distance from each vertex to the centroid produces an anomalous region which is similar in size and position to that of the synthetic model (Figure 5.13). This combination of regularization parameters was used in the initial inversion attempt as they were the most successful in the 2D case (See Chapter 4). The initial input velocity model is shown in Figure 5.2. The velocities of the deposit and the host rock calculated (or predicted) by the inversion were 2559 m/s and 2003 m/s, respectively. This corresponds quite well to the synthetic (or observed) velocities of 2500 m/s for the deposit and 2000 m/s for the host rock. The fit of the predicted data to the synthetic observed data is satisfactory. The convergence curves (i.e. the total perimeter, the total area, and the total distance from each vertex to the centroid) are well-behaved in that they show a smooth steady decrease. While the constructed model does appear to have a bit of an extra curve to it as compared with its synthetic counterpart, in general, the inversion was succesfull.

In order to properly investigate the quality of the result detailed above

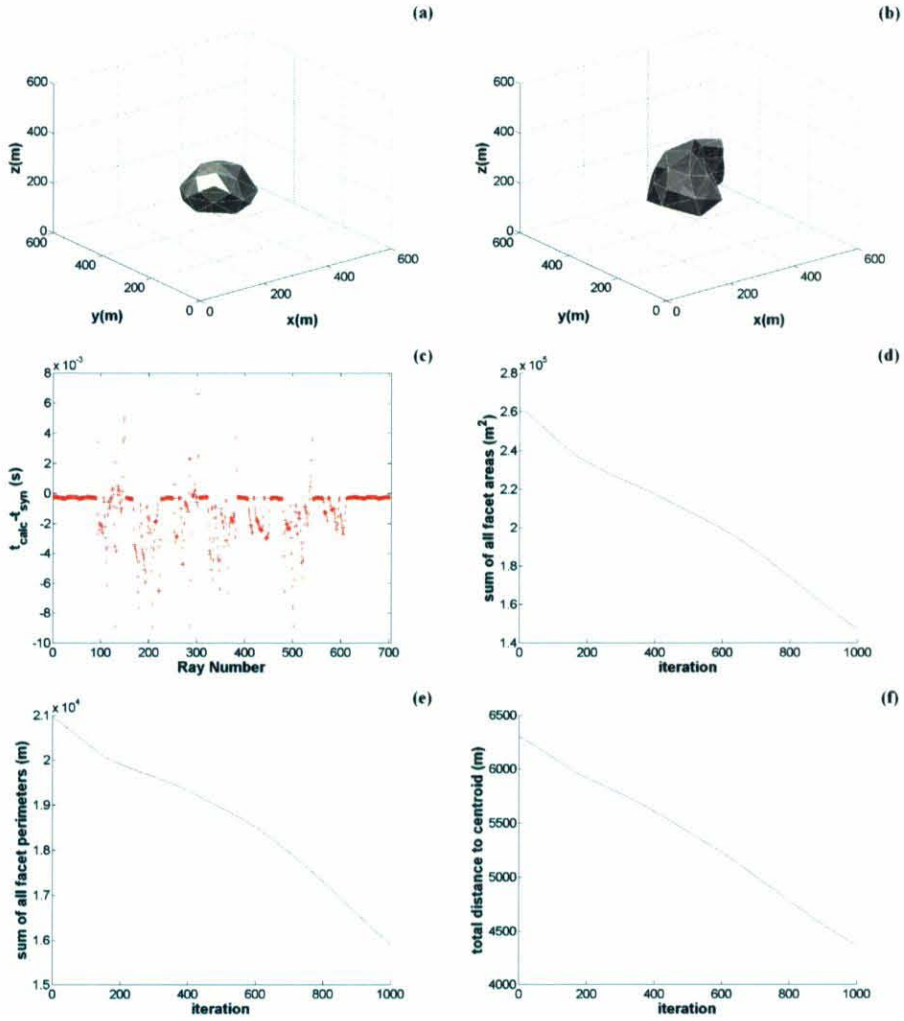

Figure 5.13: Minimum structure inversion result for a 2500m/s tessellated 3D subsurface shape embedded in 2000m/s host rock: (a) Synthetic velocity model. (b) Resultant velocity model. (c) Difference between calculated (i.e. inverted) travel-time and synthetic travel-time. (d) Sum of all facet areas trace. (e) Sum of all facet perimeters trace. (f) Total distance to centroid from each vertex trace.

and the merit of the inversion procedure, it must be compared to an inversion without regularization. This approach does not involve the minimization of any measures of model structure and employs only a simple minimization of the misfit between the observered and predicted data (Equation 2.18). After 50 iterations the synthetic model appears irregular (Figure 5.14). Upon closer inspection, the anomolous region has actually flipped inside out on itself (Figure 5.15). Also, two of the convergence curves (the total perimeter and the total area) are increasing while the one for the total distance from each vertex to the centroid is actually decreasing. This indicates there is discordance between these model properties and probably reflects the irregularity and jaggedness of the resultant velocity model. This result helps put the one obatined via a minimum structure inversion into perspective. On a relativistic scale, the minimum structure inversion preforms significantly better than if no regularization had been used.

For completness, Figure 5.16 shows the exact same minimum structure inversion except the background (or host rock) velocity is no longer a model parameter being soug!ht and is instead known. Much of the computation time is spent determining the host rock velocity and in a real-world geological setting it may be possible to determine this value prior to completing the seismic borehole survey. The difference between the two results is unremarkable. The misfit between the predicted and observed data appears to be smaller due to a flatter basline. This illusion is due to the fact that a greater number of rays pass through the host rock than the anomalous region.

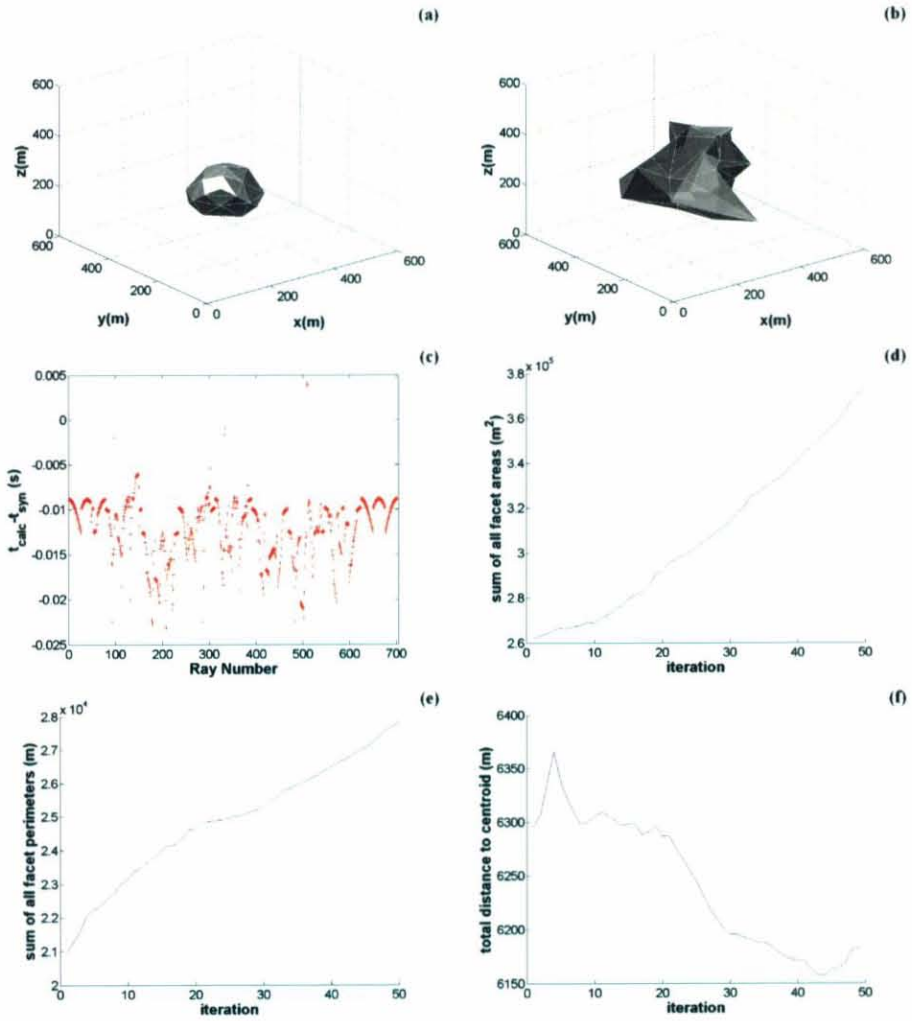

Figure 5.14: Minimization of misfit inversion result for a 2500m/s tessellated 3D subsurface shape embedded in a 2000m/s host rock: (a) Synthetic velocity model. (b) Resultant velocity model. (c) Difference between calculated (i.e. inverted) travel-time and synthetic travel-time. (d) Sum of all facet areas trace. (e) Sum of all facet perimeters trace. (f) Total distance to centroid from each vertex trace.

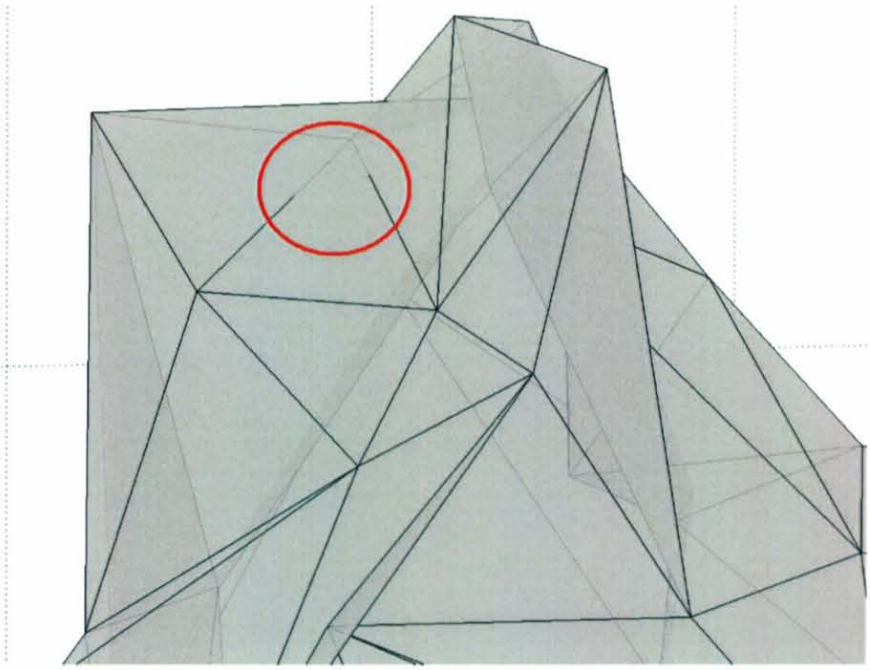

Figure 5.15: Close up of the resultant velocity model from Figure 5.14(b). The area where the triangular facets flipped inside-out is circled in red.

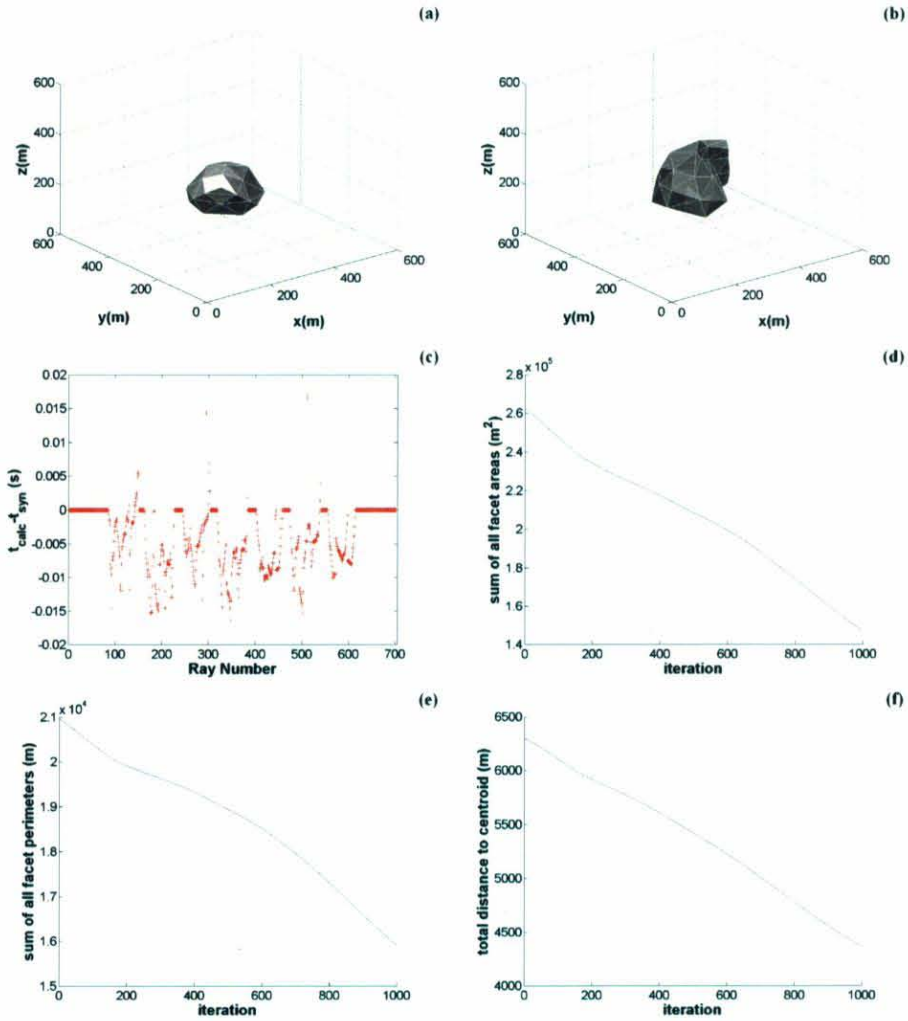

Figure 5.16: Minimum structure inversion result for a 2500m/s tessellated 3D subsurface shape embedded in a host rock of known velocity: (a) Synthetic velocity model. (b) resultant velocity model. (c) Difference between calculated (i.e. inverted) travel-time and synthetic travel-time. (d) Sum of all facet areas trace. (e) Sum of all facet perimeters trace. (f) Total distance to centroid from each vertex trace

Chapter 6

Conclusions

The preceding thesis applied a minimum structure inversion to a model parametrized by a numerically defined surface in both two and three dimensions. The position of the surface varied throughout the course of the inversion. In order to prevent the surface from turning inside out, appropriate measures of model structure were choosen. These regularization parameters included the perimeter, the area and the sum of the distances from each vertex to the models' center. The resulting 2D inversion was compared to both an l_2 and non-l_2 minimum structure inversion of a traditional voxellated model.

Models obtained using traditional implementations of minimum-structure inversion involving cellular partitioning procedures typically have a fuzzy, smeared-out appearence. This can be partially circumvented by modifying the typical minimum-structure inversion algorithm to include an l_1-type measure of model structure instead of the traditional sum-of-squares, or l_2-type measure. This generates a more blocky and piecewise constant earth model. However, these models often lack the complexity needed to describe the subsurface and tend to smear along the direction of data collection.

Defining a model using a numerically defined shape in 2D and 3D is an accepatable form of model parametrization. Regulating the inversion by using measures of model structure allows for a robust and reliable algorithm that preforms better than its non-regulated counterpart. The results are more consistent with our real or percieved knowledge of the subsurface and do not have the fuzzy, smeared-out appearence typical of traditional cellular models using sum of squares measures.

As the primary interest of this thesis is model parametrization as it applies to the inversion procedure, both the forward and inverse problems were simplified by assuming a straight raypath from source to reciever. In order to better understand as well as mimic the affect velocity variation has on the inversion procedure, future studies should incorporate ray theory into the algorithm.

There is the potential for widespread use of this inversion procedure by tweaking how the surface is numerically defined. Parametrizing a model using spherical harmonics, for example, would allow for a more smoothly varying surface as opposed to the sharp-edged, constant anomaly used in this thesis. The inversion procedure could then be applied to a much wider variety of geological situations.

Finally, the thesis showed that an inversion for a sharpe-edged, constant anomaly does a better job recovering synthetic data from a sharp, uniform subsurface feature than a minimum-structure tomographic approach. The synthetic data used is consistent with the actual geology of an ore deposit.

The resulting algorithm provides geophysicists with a more geology-specific inversion tool that out-performs its tradiational counterparts.

Bibliography

Aki, K. & Richards, P., 1980. *Quantitative Seismology*, W. H. Freeman and Co., Oxford, UK.

Bonnans, J., Gilbert, J., Lemarechal, C., & Sagastizbal, C., 2006. *Numerical Optimization Theoretical and Practical Aspects*, Springer, New York.

Burke, P., 1988. Calculating the area and centroid of a polygon, *http://local.wasp.uwa.edu.au/~pbourke/geometry/polyarea*.

Cardarelli, E. & Nardis, R., 2001. Seismic refraction, isotropic and anisotropic tomography on an ancient monument (antonino and faustina temple ad 141), *Geophysical Prospecting*, **49**, 228–241.

Červaný, V., 2001. *Seismic Ray Theory*, Cambridge University Press, Cambridge, MA.

Chander, R., 1975. On tracing rays with specified end points, *J. Geophs.*, **41**, 173–177.

Farquharson, C., 2008. Constructing piecewise-constant models in multidimensional minimum-structure inversions, *Geophyics*, **73**, K1–K9.

Fletcher, R., 1987. *Practical methods of optimization (2nd ed.)*, John Wiley and Sons, New York.

Glassner, A., 1989. *An Introduction to Ray Tracing*, Academic Press Limited, London, UK.

Gubbins, D. & Julian, B., 1977. Three dimensional seismic ray tracing, *J. Geophys.*, **43**, 95–114.

Iyer, H. & Hirahara, K., 1993. *Seismic Tomography: Theory and Practice*, Springer, Oxford, UK.

Jacob, B. R., 1970. Three dimensional seismic ray tracing in a laterally heterogeneous spherical earth, *J. Geophys. Res.*, **75**, 6685–6689.

Kearey, M., Brooks, M., & Hill, I., 2002. *An Introduction to Geophysical Exploration*, Blackwell Science Ltd., Oxford, UK.

Lopshits, A., 1963. *Computation of area of oriented figures*, D C Health and Company, Boston, MA.

Mao, W. & Stuart, G., 1997. Rapid multi-wave-type ray tracing in complex 2d and 3d isotropic media, *Geophyics*, **62**, 298–308.

Mathematica, 2005. *Mathematica Edition: Version 5.2*, Wolfram Research Inc., Champaign, Illinois.

Matlab, 2005. *Matlab Edition: Version 7.1*, The Mathworks Inc., Natick, MA.

Nicholson, K., 2003. *Linear Algebra with Applications*, McGraw-Hill Ryerson Limited, Ontario, Canada.

Nocedal, J. & Wright, S., 1999. *Numerical Optimization*, Springer, New York.

Nolet, G., 1987. *Seismic Tomography*, D. Reidel Publishing Company, Dordrecht, Holland.

Pereyra, V., Lee, W., & Keller, H., 1980. Solving two-point seismic-ray tracing problems in a heterogeneous medium, *Bull. Seismol. Soc. Am.*, **70**, 79–99.

Sheriff, R. & Geldart, L., 1995. *Exploration Seismology*, Cambridge University Press, Cambridge, UK.

Thurber, C., 1987. Analysis methods of kinematic data from local earthquakes, *Rev. Geofis.*, **24**, 793–805.

Um, J. & Thurber, C., 1987. A fast algorithm for two-point seismic ray tracing, *Bull. Seismol. Soc. Am.*, **77**, 972–986.

Vidale, J., 1988. Finite-difference calculation of travel times, *Bull. Seismol. Soc. Am.*, **78**, 2062–2076.

Wesson, R., 1971. Traveltime inversion for laterally inhomogeneous crustal velocity models, *Bull. Seismol. Soc. Am.*, **61**, 729–746.

Appendices

Please see attached compact disc for subsequent appendices. Each appendix corresponds to a file folder. The contents of each folder are given below.

Appendix A

Inversion 225 cell mesh

Inversion 3600 cell mesh

Appendix B

l1 type inversion 3600 cell mesh

Appendix C

Background velocity unknown

↪ Forward problem 6 segments

↪ Jacobian calculation 6 segments

↪ Inversion minimization of misfit 6 segments

Background velocity known

↪ Forward problem 6 segments

↪ Jacobian calculation 6 segments

↪ Inversion minimization of misfit 6 segments

Appendix D

Background velocity unknown

↪ Forward problem 10 segments

↪ Jacobian calculation 10 segments

↪ Minimum structure inversion 10 segments

Background velocity known

↪ Forward problem 10 segments

↪ Jacobian calculation 10 segments

↪ Minimum structure inversion 10 segments

Appendix E

Background velocity unknown

↪ Forward problem 20 segments

↪ Jacobian calculation 20 segments

↪ Minimum structure inversion 20 segments

Background velocity known

↪ Forward problem 20 segments

↪ Jacobian calculation 20 segments

↪ Minimum structure inversion 20 segments

Appendix F

3D model parametrization

↪ mesh_refine

↪ mesh_refine_tri4

↪ mesh_refine_tri6

↪ sphere_project

↪ sphere_tri

Appendix G

Minimization of travel time 3D

↪ Forward problem for a sphere

↪ Forward problem minimization of travel time tessellated sphere

↪ Fermat's Principle

Shooting method 3D

↪ Forward problem shooting method 3D

Appendix H

3D numerically defined surface

↪ Forward problem 3D

↪ Jacobian Calculation 3D

↪ Minimum structure inversion 3D tessellated surface